12-14-2023

Characterizing the Evaporating Droplets over Heterogeneous Wettability Surfaces

Xi Li
xl1832@rit.edu

RIT

Title of My Dissertation

Characterizing the Evaporating Droplets over Heterogeneous Wettability Surfaces

by

Xi Li

A Dissertation Submitted in Partial Fulfillment of the Requirements for the Degree of Doctor of Philosophy in Engineering

Kate Gleason College of Engineering

Rochester Institute of Technology

Rochester, NY

December 14, 2023

Characterizing the Evaporating Droplets over Heterogeneous Wettability Surfaces

Xi Li

Advisor

Dr. Michael Schertzer

Committee

Dr. Blanca Lapizco-Encinas

Dr. Kara Maki

Dr. Kathleen Lamkin-Kennard

Abstract

This work investigates deposition patterns left by evaporating particle-laden droplets on heterogeneous surfaces with spatially varying wettability. Spatial differences in receding contact angles give rise to scalloped-shaped contact lines. During evaporation, the contact line recedes in one location and remains pinned in another. This non-uniform contact line recession results in particle self-assembly above areas where the contact line remains pinned, but not where it recedes. This behavior is fairly robust across a variety of particle sizes, concentrations, and device geometries. We hypothesize that particle self-assembly in these cases is due to the competition between particle diffusion and the evaporative-driven advective flow. Diffusion appears to be more pronounced in regions where the contact line recedes while advection appears to be more pronounced near the pinned portion of the contact line. As such, particles appear to diffuse away from receding areas and toward pinned areas where advection transports them to the contact line. The distribution of particle deposition above the pinned regions is influenced by the particle size and concentration of particles in the droplet. Similar to homogeneous surfaces, deposition is more prevalent at the pinned portion of the contact line for smaller particles and lower concentrations, and more uniformly distributed across the entire pinned region for larger particles and higher concentrations. A better understanding of this process may be beneficial in a wide variety of particle separation applications like printing, cell patterning, biosensing, and anti-icing.

Table of Contents

List of Figures

List of Tables

Nomenclature

Symbol	Meaning
D	diffusion constant
E	electric field
F_e	force of the particles from the electric field
F_S	strokes-type viscous force
H_0	initial height of the droplet
$\hat{I}_{i,j}$	normalized grayscale intensity
$\bar{I}_{p,k}$	average grayscale value
$\bar{I}_k$	average grayscale value for the k^{th} section
I_B	average background intensity
I_{max}	maximum intensity
k_B	Boltzmann's constant
L_g	gap width
L_p	printed width
$\overline{IG}$	average grayscale intensity across the entire gap region
$\overline{IP}$	average grayscale intensity across the entire printed region
q	charge of the particle
r_p	radius of the particle
t	time
T	temperature
t_{evap}	evaporation time
u_i	characteristic interface velocity
V	voltage
$\dot{x}_p$	characteristic diffusion rate
x_p	characteristic diffusion distance
η	viscosity of the solvent
$\theta_{g,r}$	receding contact angel above the gap regions

$\theta_{p,r}$	receding contact angel above the printed regions
$\theta_g(t)$	local contact angle above the gap regions
$\theta_p(t)$	local contact angle above the printed regions
π	pi
Ω_p	p-th segmented into rectangles

Abbreviation	Meaning
AC	alternating current
CCA	constant contact angle
CCD	constant contact diameter
DC	direct current
DEP	dielectrophoresis
EP	electrophoresis
PDMS	polydimethylsiloxane
PET	polyethylene terephthalate
PS	polystyrene

1 Introduction

1.1 Surface wettability

Surface wettability is a critical parameter for a wide range of applications including: heat transfer enhancement[1], water harvesting from fog[2], [3], design of anti-microbial surfaces[4], separation of oil and water[5], [6], printing[7], and fabricating antibacterial surfaces in medical and dental implants[8], [9]. Wettability is usually characterized by static measurements of the contact angle of a fluid interface on a surface at the three phase contact line shown in Figure 1.1. From Figure 1.1, there are three phases: the gas phase, the liquid phase, and the solid phase. The contact line is at the connection of these three phases. The contact angle θ, between the liquid phase and the solid phase, is shown from the side view in Figure 1.1. However, dynamic measurements of advancing and receding contact angles, adhesive strength, and pinning forces can also differ on surfaces with similar initial contact angles. Surface wettability is generally a function of chemical interactions between the fluid and the surface[10], and of the physical properties (i.e., roughness) of the surface[7]. Chemical properties of a surface can be controlled by a number of means including: UV irradiation[11], plasma treatment[12]–[14], molecular grafting[15], [16], and direct printing of functional materials[7], [17]. Physical changes on a surface are generally achieved through deliberate patterning of micro- and nano-scale roughness using multiple techniques including: 3D printing[18], [19], reactive ion beam etching[20], [21], and laser ablation[22], [23]. The apparent wettability of a surface can also be dynamically altered through the creative application of thermal gradients[24], surface acoustic waves[25], and electric fields[26]. Creative use of non-uniform chemical and physical techniques has led to functional surfaces with heterogeneous wettability for a

wide range of applications including: printing[17], cell patterning[27], bio sensing[28], fog harvesting[29], and preventing ice formation or anti-icing[30].

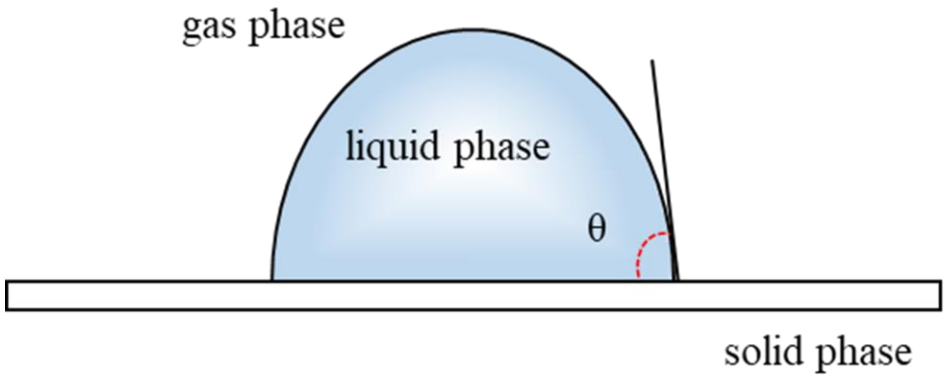

Figure 1.1: Contact angle and contact line description. The blue sphere cap is the liquid phase. The black box under the liquid is the solid phase. Outside the liquid phase is the gas phase. θ is the contact angle which between the liquid phase and the solid phase from the side view.

1.1.1 The effect of physical and chemical changes on surfaces

The physical properties of the surfaces could be manipulated in many different ways. The surface roughness is usually different over different kinds of surfaces. The study of changing the morphology of the surface and the media of the surface has been very popular recently. In one example of physical alteration of surface wettability, Mohammad Karim et al. created rough hydrophobic Teflon plates to examine the spreading dynamics of polyethylene glycol (PEG)[31]. They saw an increase in the receding contact angle for a 20% PEG solution as the roughness height increased from $38\ \mu m$ ($53.3°$) to $86\ \mu m$ ($59.6°$), and then $305\ \mu m$ ($64.9°$)[31]. Recent investigations examining inkjet-printed microfluidic devices reported that printing conductive elements and coating them with thin dielectric layers (~$5\ \mu m$) increased the roughness on the upper surface even after polymer coating[32]–[34]. In particular, Bernetski et al. reported that inkjet printed features had a root mean square (RMS) roughness on the order of $400\ nm$ and $200\ nm$ before and after spin coating $4.5\ \mu m$ to $6.5\ \mu m$ of the photoresist SU-8, respectively. The after-coating roughness observed here is of a similar order to the change in roughness reported by Mohammad Karim et al. This suggests that this technique may offer a mechanism to locally control surface wettability.

Chemical properties of the surface can be manipulated by UV irradiation, plasma treatment, printing, and so on. Surfaces with heterogeneous wettability exhibit spatial variations in their interactions with fluid interfaces based on local differences in wettability[10]. These local differences in wettability can promote the self-assembly of functional materials, like hydrophobic molecules, held in suspension in carrier fluids as

they evaporate on these heterogeneous surfaces[35]–[37]. For example, Liu et al. are able to create conductive features on the order of 1 μm by evaporating a gold nanoink on a polymer surface with heterogeneous wettability prepared using a parallel vacuum ultraviolet technique[11]. The techniques of changing the physical and chemical properties of the surface to make a functional surfaces are widely used in the microfluidic field.

1.2 Evaporation of microdroplets

Functional surfaces are defined as surfaces that can provide new properties for new applications[38]. The functional surfaces are very important to the wettability of how the liquids behave on a surface. The differences in components and the roughness are both key factors in the functional surfaces[39]. The study of particles over functional surfaces has drawn great attention in the biomedical, mechanical, and industrial fields[40]. Since 1980, people have found that it is costly in materials, fluids, and devices when downsizing to the micro or nano size[41]. At the same time, downsizing can also increase the sensitivity and convenience when testing multiple samples. This trend to downscale the droplets and devices is also called microdroplets in microfluidics.

Microfluidics is a relatively new field of study that emerged in the early 90's [1][2], sparking scientific interest in the development of devices for fluid flow at the microscale [2][3]. Previously, thermodynamic processes usually taking up hours or days, such as chemical and biological reactions, including isolation and separation, are now accelerated to a few minutes when reduced to the micron scale as the total demand of the materials reduces drastically in the microfluidics [44]. Indeed, microdevices are very useful since they employ and control small volumes of fluid and response fast at a smaller scale [5][6]. Microfluidics has been used to "shrink" other known devices for various applications: valves, sensors, mixers, etc. [47]. It is described as an enabling technology in the biological science field, that may open doors to the application of microfluidics to single-cell assays, phenotypic screens, and gene-expression profiling, as well as improving the performance of bioanalytical detection devices.

1.2.1 Particle transport and deposition in evaporating droplets

There has been significant interest in the transport and deposition of particles in evaporating droplets in recent years[49], [51], [52]. An understanding of this complex physical phenomenon has drawn considerable attention in a variety of fields including industrial, chemical, and biomedical fields, especially in applications including medical diagnostics, health monitoring, and cell biology [42]–[44]. Specific examples of particle transport and/or deposition in evaporating droplets include inkjet printing. When ink droplets dry, the ink particles deposit and form patterns completing the printing process[33]. For polymer depositions, the transport of the molecules inside the droplet is related to the contact line wettability[53]. In medical diagnostics, the blood strain has been studied to provide disease signals[54].

For particle transport and deposition in evaporating droplets, the dynamics of the droplet on the substrate during evaporation have been studied for decades in an effort to avoid the coffee-ring effect, an enhance the edge effect, notably in the inkjet printing industrial [9], [11], [12]. This kind of coffee-ring pattern is the result of the contact line pinning and the interplay of surface tension and the evaporation flux [56]–[59].

During evaporation, there are various competing effects inside the droplet to form the deposition patterns, and some of them are shown in Figure 1.2. The radial flow shown in figure 1.2A could bring particles to the liquid-solid contact line during evaporation. This flow is caused by the different evaporation rates along the surface. The scale of radial flow can be predicted as $V_{rad} \sim J/\rho$, in which J is the evaporation flux and ρ is the fluid density, from Larson et al.[60]. The Marangoni recirculation, shown in Figure 1B, could either bring the particles to the contact line or carry them back to the center of the droplet. The

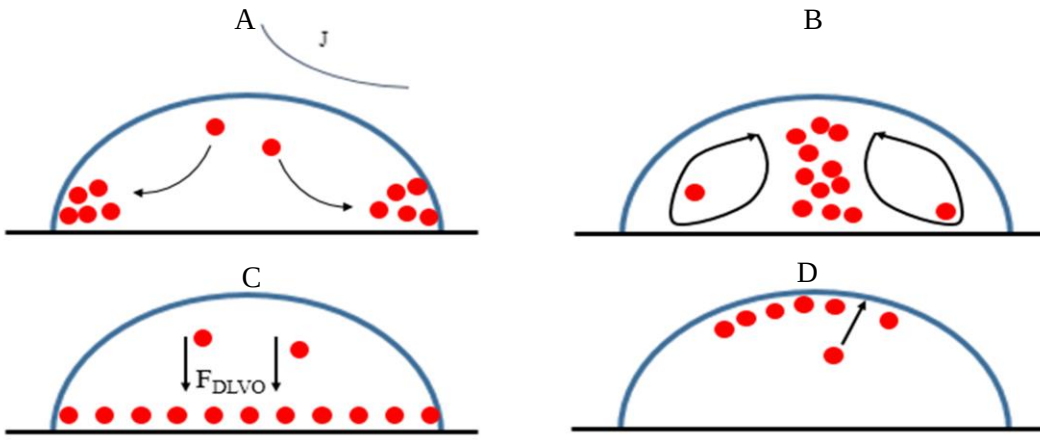

Figure 1.2 : Four different convective mechanisms compete during evporation (A) the radial flow which is driven by evaporation gradient, (B) the Marangoni recirculation which is driven by the surface tension gradient, (C) the DLVO force which is between the substrate and the particles, and (D) the surface caputure effect which is related to the top surface movement.

magnitude of the Marangoni recirculation velocity is determined by the surface tension gradient [60]. The DLVO force, named after Boris Derjaguin and Lev Landau, Evert Verwey, and Theodoor Overbeek, is between the particles and the substrate. This force is the combination of the electrostatic force and the Van der Waals force. Depending on the particles and the surface charge, the DLVO force could either attract the particles to the substrate or push them away from the substrate[61]. Sometimes, the liquid-gas interface

could capture the particles during evaporation shown in Figure 1.2D. If the interface moves down faster than the diffusion of the particles, many particles would be captured by the interface during evaporation to form a more uniform deposition pattern[62]. Moreover, many other factors could influence the movement of the particles during evaporation. For example, the size and the concentration of the particles, the temperature and the humidity of the environment, the pH of the solution, and so on[63]. In conclusion, there are vast competing factors that may influence the movement of the particles during evaporation worthy of studying.

Previous investigations have demonstrated that deposition patterns can be altered through the application of an electric field or "electrowetting", consisting of applying direct or alternating voltages to a surface [64], [65]. Improved deposition uniformity is observed when a DC field is applied to evaporating droplets carrying TiO_2 particles [64]. With the AC field, the oscillation of the water droplet due to the sliding transition is considered to change the hysteresis [66]. Also, the coffee-ring effect could be suppressed with high frequency as the thermal mixing effect happened at the liquid-gas interface [65]. Moreover, the dielectrophoresis (DEP) under the AC has been shown to have the ability to separate particles in a close microfluidic environment [67].

1.2.2 Modes of evaporation

Although so many properties we can change and so much competition inside the droplet during evaporation, some common phenomena can be predicted. The contact line

mobility and the contact angle change can be predicted during evaporation. In general, particle assembly within evaporative droplets is determined by heat, momentum, and mass transport processes; contact line dynamics; and interactions of the particles with themselves, the interface, and the substrate[24], [68]. Comprehensive review articles on this topic have been written by Larson[24], Sefiane[69], and Patile and Bhardwaj[70]. This work considers microliter-sized particle-laden droplets evaporated in stagnant, ambient air with no additional thermal effects. In these drying conditions, a typical evaporating droplet on a homogeneous substrate will move through three modes (shown in Figure 1.3) during evaporation: (i) constant contact diameter (CCD), where contact angle decreases and the contact line remains pinned (also referred to as constant contact radius[71], or constant contact line[72]); (ii) constant contact angle (CCA), where contact diameter decreases; and (iii) mixed mode, where both the contact diameter and contact angle decrease[50], [73].

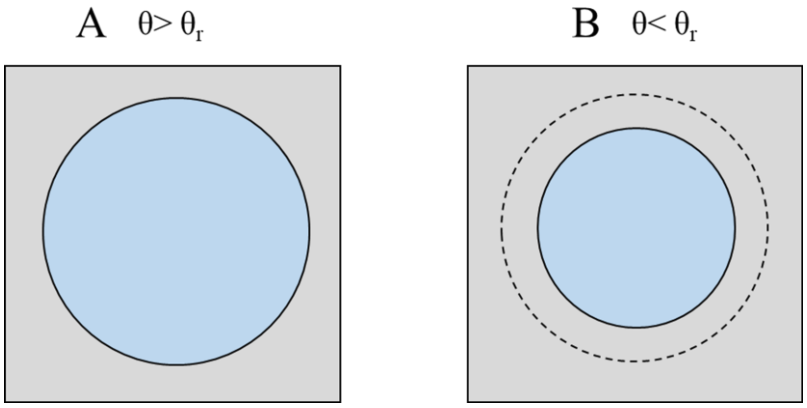

Figure 1.3: Modes from top-view during evaporation (A) constant contact diameter (CCD), where contact angle decreases and the contact line remains pinned; (B) constant contact angle (CCA), where contact diameter decreases. θ_r is the receding contact angle.

How the droplet moves between different modes of evaporation is influenced by several factors including, but not limited to: surface wettability[74]; surface defects and non-homogeneities that cause local differences in the receding contact angle[75]; and the presence[76], concentration[77], and physical properties of particles in the droplet[78]. During evaporation, the droplet can also enter a stick-slip regime where the contact line periodically pins (sticks) and depins (slips). This stick-slip behavior is often attributed to surface defects[77], heterogeneities[74], or the presence and physical properties of particles at the contact line[78].

The contact line dynamics determine the fluid flow within the evaporative droplet. In the simple case, where a millimeter-sized droplet of water evaporates slowly in ambient air with a pinned contact line (CCD mode), there is a competition between an evaporation-driven radially outward flow and a recirculating Marangoni flow[50]. When the outward radial flow dominates, particles are collected at the contact line. When the Marangoni flow dominates particles can collect in the center of the droplet if the thermal conductivity ratio between the substrate and the fluid is greater than two[50], [79], [80]. Deegan et al. observed a stagnation point beyond which the inward, recirculation flow near the center of the droplet is an outward flow[50]. This stagnation point has been observed by other researchers[81]. But when the contact line is receding, the fluid in the droplet tends to recirculate at a reduced velocity compared to the pinned contact line case[82]. Overall, advection from evaporative-driven flows is a critical variable governing how particles collect and deposit on the substrate during drying[83].

1.2.3 Particle transport related to evaporation modes

Particle transport in evaporating droplets can be affected by the particles themselves. Prior works have varied particle shape[84], [85], type[86], charge[87], size[51], and concentration[69], [88] and all can play a role in transport and deposition. For example, particle shape can be used to affect particle transport and deposition by altering how particles arrange themselves on the air-water interface during evaporation[89], [90]; particle transport can be affected by surface and particle charges results in Derjaguin, Landau, Verwey, and Overbeek effects that combine van der Waals' and electrostatic forces between particles and surfaces[87], [91]; and particles that are denser than the liquid they are suspended in are likely to sink to the substrate before being carried to the contact line by advection[63], [90], [92]. The present study focuses on particle concentration and size. Increased particle concentration has been shown to increase contact line pinning, which can delay or prevent the transition from the CCD evaporative mode to the CCA mode[3], [69], [88], [93]. Many works have also shown that smaller particles ($< 1\ \mu m$) are more likely to increase the pinning force at the contact line[10], [50], [78]. This also delays transition from the CCD to CCA modes.

Particle size has also been shown to alter deposition patterns left by particles in evaporating droplets by altering the interplay between particle diffusion and advection to a pinned contact line when outward radial flow dominates[62], [93]. These works suggest that particles are more likely to be captured on the descending interface when the characteristic particle diffusion rate is less than the average interface velocity. But when

the diffusion rate is larger than the interface velocity, the radially outward flow in the droplet is more likely to bring particles to the contact line where they form a ring-like deposition pattern. Here, the characteristic diffusion rate ($\dot{x}_p$) is estimated by first defining a characteristic diffusion distance (x_p) traveled in a given amount of time (t). This estimation is given by

$$x_p = 2\left(\frac{Dt}{\pi}\right)^{1/2} \quad (1)$$

where the diffusion constant (D) is estimated from the Stokes-Einstein relation ($D = k_B T/6\pi\eta r_p$, k_B is Boltzmann's constant, T is the temperature, η is the viscosity of the solvent, and r_p is the radius of the particle), and t is the characteristic time[94]. A characteristic diffusion rate ($\dot{x}_p$) is determined by setting $t = 1$ in eq 1 to estimate the characteristic distance a particle is expected to travel in one second. The characteristic interface velocity (u_i) can be estimated as

$$u_i = H_0/t_{evap} \quad (2)$$

where H_0 is the initial height of the droplet and t_{evap} is the evaporation time. As particle size decreases, D in eq 1 increases. This leads to an increase in $\dot{x}_p$. If particle effects do not appreciably alter drying time, then u_i would remain approximately constant and the smaller particles would be expected to more easily diffuse away from the descending interface and carried to the contact line to form a ring pattern[62], [93]. Conversely, larger particles would diffuse more slowly and be more likely to be trapped on the descending interface to form a more uniform pattern[62], [93].

1.3 Heterogeneous wettability

A functional surface with heterogeneous wettability is also called heterogeneous surfaces[74]. Compared with homogeneous surfaces, heterogeneous surfaces have unique nonuniformity wettability influencing the contact line motion. Heterogeneous wettability may result in multiple different patterns. With desired geometries, for example, the heterogeneous wettability may result in the incorporation of hydrophilic regions, hydrophobic regions, and gradient regions[74]. Both chemical and physical methods to change the surface properties could make heterogeneous wettability surfaces. Recently, there has been used in a variety of wide applications including: cell patterning, printing, and biosensing[7], [16], [28].

Heterogeneous dewetting of the contact line during evaporation is likely to alter the interplay between the effects typically governing particle transport and deposition in evaporating droplets. In particular, particle advection on these types of surfaces is likely to be heterogeneous as the flow pattern in the droplet changes depending on whether the contact line is pinned or receding[26], [66], [77], [95]. The change in these advective effects may also change the relative importance of particle-related effects under particular evaporation conditions.

The design of a heterogeneous surface can result in the preferential recession of the contact line on more hydrophobic areas of the device. For example, Jansen et al. observed non-uniform contact line recession when elongated droplets are evaporating on chemically

striped surfaces. They found that contact line recession occurred more easily parallel to the strips than perpendicular to them[96]. Liu et al. demonstrated particle self-assembly from evaporating droplets of gold nano ink onto a heterogeneous surface with lined features, characterized their electrical performance, and created design rules for device design based on device geometry[11]. He et al. examined the used of heterogeneous wettability to promote particle self-assembly on devices with rectangular hydrophilic patches on a hydrophobic substrate[14]. They observed that the evolution of evaporative modes during diffusion-limited evaporation is different than on heterogeneous surfaces[14]. They reported droplets passing through four different modes of evaporation: constant contact radius, constant contact angle, pattern-pinning, and moving contact line[14]. These differences in droplet evaporation likely lead to the promotion of particle self-assembly on the more hydrophilic areas of the devices that exhibit heterogeneous dewetting[11], [17]. These works[11], [14] also demonstrate that creative patterning of surfaces with heterogeneous wettability can be used to control particle self-assembly in evaporating droplets.

A deeper understanding of particle transport and deposition during diffusion-limited evaporation of droplets on heterogeneous surfaces is needed to improve the design of functional surfaces that leverage heterogeneous dewetting. This investigation tests the hypothesis that heterogeneous dewetting can be achieved on low-cost inkjet printed devices coated by a thin polymer film. In doing so, it aims to deepen the understanding of particle self-assembly in diffusion-limited evaporating droplets on heterogeneous wettability surfaces that use striped patterns of differing wettability. It seeks to understand how the

droplet passes through relevant modes of evaporation and how those modes affect particle transport and deposition as the droplet evaporates. To do so, it will examine evaporating droplets on surfaces with heterogeneous wettability over a range of particle sizes, surface geometries, and particle concentrations.

2 Experimental methodology

The experimental setup for this investigation consisted of a device with heterogeneous wettability, a particle-laden droplet, and two imaging systems. The manufacturing of the device is first explained followed by the setup and implementation of the experiments.

2.1 Heterogeneous devices

The heterogeneous devices consisted of a $50\ mm \times 75\ mm$ piece of inkjet-printed media fixed to a glass slide of the same dimensions (Figure 2.1A). The features (Figure 2.1B) are printed onto flexible polyethylene terephthalate (PET) media (Novacentrix Novele) by an Epson Stylus C88+ printer loaded with silver nano ink (Novacentrix JS-B25P) as in Bernetski et al[34]. The media is then carefully attached to the glass substrate (Corning, $50\ mm \times 75\ mm$) with double side tape. A $6\ \mu m$ layer of PDMS (Gelest, sPDMS: spin coatable reprographic silicone with mix ratio 100:1) is then spun onto the device. The spin coater (Laurell WS-650MZ-23NPPB) is set at $1000\ rpm$ for $10\ min$. After spincoating, the device is baked on a hot plate at $80°C$ for four hours.

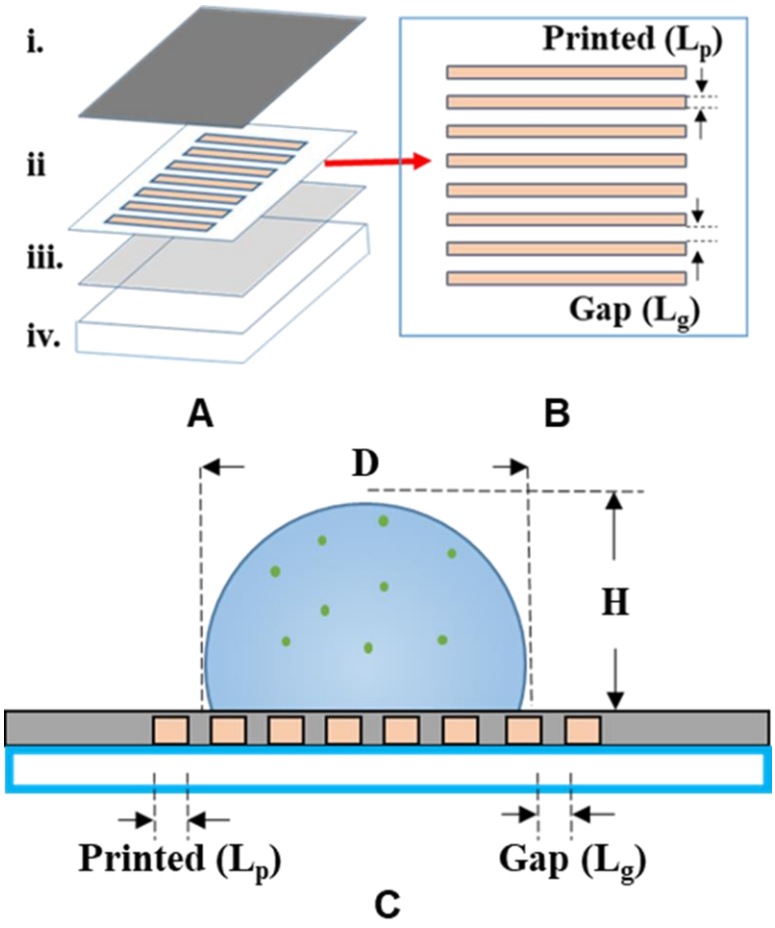

Figure 2.1: Isometric view of the layers of the device. (A) isometric exploded view of the layers of the device: i) PDMS coating; ii) prints on the PET film; iii) double side tape; iv) glass slide. (B) top view of the device surface with printed patterns. (C) side view of the droplet during evaporation.

2.2 Inkjet printing methods

The low-cost inkjet printing devices are fabricated based on the methods from Dixon and Burkhart et al[33], [34]. The printer is a commercially available desktop inkjet printer Epson Stylus C88+ shown in Figure 2.2. The printer is about $120 USD and is considerably low compared with the cleanroom process. The ink cartridges are replaceable with silver nano ink (Novacentrix JS-B25P) for printing the patterns. The printing media

are transparent sheets with flexible polyethylene terephthalate (PET) from Novacentrix Novele. The sheets are loaded into the paper feed of the printer just like normal white paper.

The printed patterns are designed in Adobe Illustrator with actual size. The inkjet-printed patterns in this investigation are all rectangles with printed widths (L_p) of sizes 100 μm, 200 μm, or 300 μm separated by gap widths (L_g) of sizes 100 μm, 200 μm, or 300 μm (Figure 2.1B). In all cases, the experimental area is a square region on the order of 2000 μm x 2000 μm shown in Figure 2.1B. The printing settings are listed in Table 2.1. As the grayscale mode is used for printing, the black cartridge is filled with silver ink while other cartridges are empty. Nozzles are checked each time before printing to keep good printing status. After printing, the black cartridge is replaced with a cleaning solution. For the cleaning process, the printer kept printing black squares on A4 white paper until no silver ink is left in the nozzles.

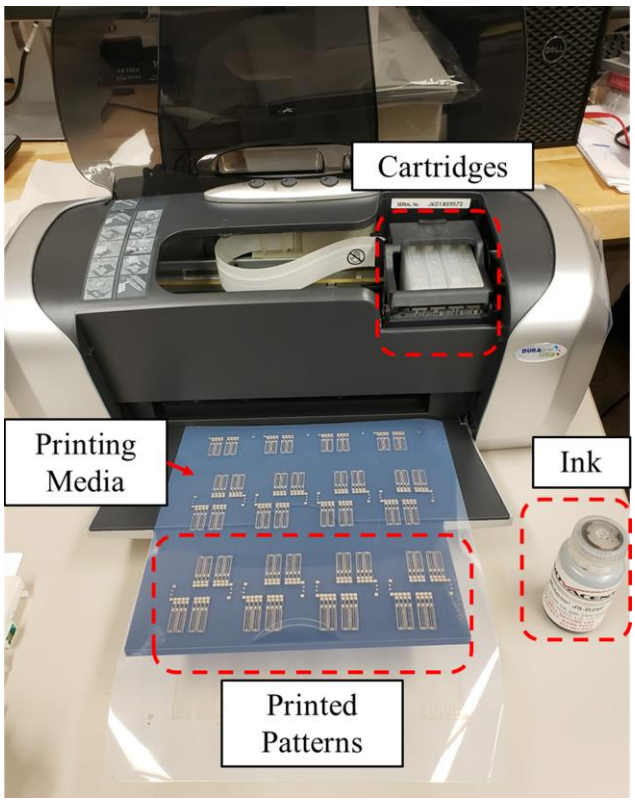

Figure 2.2: The whole view of the inkjet-printer. The red boxes are the ink, printed patterns, and the printer cartridges.

Parameters	Setting
Paper Type	Matte (heavyweight)
Print Quality	Best Phote
Grayscale	On
High speed	Off

Table 2.1 : Parameters used during printing.

2.3 Droplets and environment

The droplets used in this investigation contained fluorescent polystyrene (PS) particles ($0.002\ wt\%$, $0.02\ wt\%$, and $0.2\ wt\%$) from $0.02\ \mu m$, $0.1\ \mu m$, $1\ \mu m$ to $6\ \mu m$ diameter (FluoSpheres carboxylate-modified microspheres) in deionized (DI) water (MAXTITE typ I, 1.237 $\mu S/cm$). A stock particle solution is mixed in a sonicator (Branson 2800) for five minutes and then drawn by pipette before each test to ensure good dispersion. The particle-laden droplet ($3\ \mu L$) is then deposited onto the PDMS coated inkjet-printed device. Evaporation conditions are similar to the $24 \pm 1.2\ °C$ and $47\% \pm 12\%$ (the error bars are calculated from several days with 95% confidence) relative humidity reported by Burkhart et al.[62] measured with Inkbird THC-4 data logger.

2.4 Imaging systems

Experiments are performed to observe and analyze (i) the evolution of the droplet interface during evaporation and (ii) the resulting deposition pattern. Top and side-view images are captured using three separate optical systems: a fluorescent microscope, a goniometer, and a scanning electron microscope (SEM). The top-view time-series, bright field, and fluorescent images are recorded with a camera (QIClick-R-F-M-12 1392x1040 pixels) mounted on a Zeiss Stereo Discovery v12 microscope. Side-view images during evaporation are captured using a Ramé-Hart 250 goniometer (Figure 2.3) with a camera (BASLER acA640-90 μm 659x494 pixels). Contact angles are measured from transient images (one frame per second) captured using a Ramé-Hart Goniometer (250-U1) equipped with DROPimage Advanced software (version 2.8.02). SEM images of deposition patterns are taken using a JEOL IT100LA scanning electron microscope.

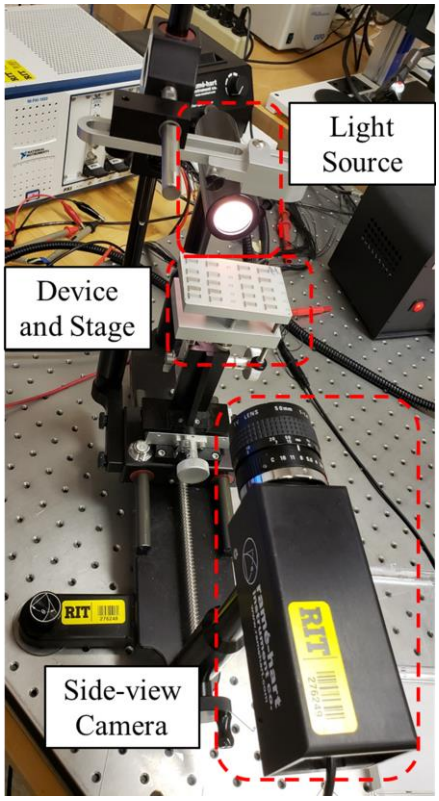

Figure 2.3: Rame-Hart imaging system with actual slide on the stage. The red box refers to the light source, devices and stage, and side-view cameras respectively

2.5 Imaging analysis

Fluorescent eight-bit images of deposition patterns are analyzed in ImageJ to characterize pixel intensity over both gap and printed regions on the device. The normalized grayscale intensity at a given pixel ($\hat{I}_{i,j}$) is defined as

$$\hat{I}_{i,j} = \max\left(\frac{I_{i,j}-I_B}{I_{max}-I_B}, 0\right) \quad (3)$$

where $I_{i,j}$ is the measured intensity at the (i,j) pixel, I_B is the average background intensity, and I_{max} is the maximum intensity measured at a given pixel (255). The average background intensity (I_B) is calculated by averaging the grayscale value of several areas of interest outside the deposition pattern.

Two different measurements of the intensity of the gap regions are analyzed. First, the droplet's gap regions are segmented into rectangles (Ω_p) as shown in Figure 2.4A. Each rectangular strip (Ω_p for $p = 1,..,N$) is then subdivided into 40 sections ($\Omega_{p,k}$ for $k = 1,..,40$), or sections of 2.5% of the total length, as shown in Figure 2.4B. The average grayscale value ($\bar{I}_{p,k}$) in each of these sections is then calculated as

$$\bar{I}_{\boldsymbol{p,k}} = \frac{\sum_{(i,j)\in\Omega_{p,k}} \hat{I}_{i,j}}{n_{p,k}} \quad (4)$$

where $\Omega_{p,k}$ is the set of pixels in the k^{th} section of the p^{th} rectangular region and $n_{p,k}$ is the total number of pixels in $\Omega_{p,k}$. Then the average grayscale value for the k^{th} section across all gap regions ($\bar{I}_k$) is calculated as

$$\bar{I}_k = \frac{\sum_p \bar{I}_{p,k}}{N}. \quad (5)$$

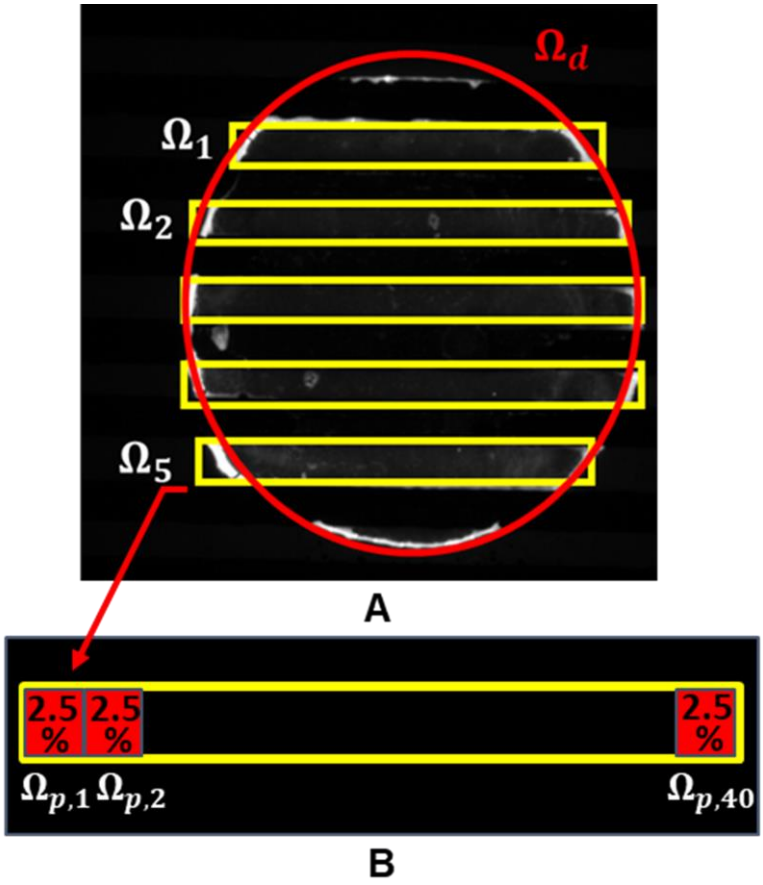

Figure 2.4: A sample fluorescent image of a deposition pattern with 0.02 μm PS particles. (A) Deposition image with 5 yellow rectangular gap regions. (B) The subdivision of one of the rectangular gap regions into 40 sections each 2.5% of the total length.

In summary, $\bar{I}_k$ quantifies the average particle concentration in the gap regions as a function of spatial location relative to the contact line. The second statistic created

quantifies the percentage of particles deposited in the gap regions. The average grayscale intensity across the entire gap region ($\overline{IG}$) is calculated as

$$\overline{IG} = \frac{\sum_{(i,j)\in\Omega_g} \hat{I}_{i,j}}{\sum_{(i,j)\in\Omega_d} \hat{I}_{i,j}} \quad (6)$$

where $\Omega_g = \bigcup_p \Omega_p$ is the set of pixels in the rectangular gap regions and Ω_d is the set of pixels in the deposition pattern (see Figure 4A). Intensity fraction over the printed region ($\overline{IP}$) can be defined in a similar manner, using the set of pixels over the printed region in place of those over the gap, $\overline{IG} + \overline{IP} \approx 1$.

3 Surface characterization

Spatial differences in wettability can arise from chemical or physical differences on the terminal surface. Since the entirety of the device is coated in PDMS, it is assumed that the chemical makeup of the terminal surface is homogeneous. Physical heterogeneity is characterized by measuring surface roughness using an NANOVEA ST400 profilometer. The root mean square (RMS) roughness is $0.326 \pm 0.012\ \mu m$ and $0.193 \pm 0.011\ \mu m$ (the error bars are calculated from 3 different trials with 95% confidence) above the printed and non-printed regions, respectively. The difference in roughness on these surfaces is similar to that seen in previous works, such as Mohammad Karim et al[31].

Surface wettability is first characterized by examining the initial and receding contact angles on (i) a device consisting of a large printed region (Figure 3.1A) and (ii) a device with no printed regions (Figure 3.1B). The initial contact angle of a particle-free droplet on the printed surface is approximately $131.7°$ over the printed region and $113.4°$ over the gap region (Figure 3.1C). The difference in receding contact angles is larger, with a value of $77.3 \pm 2.5°$ above the printed areas ($\theta_{p,r}$), but only $45.0 \pm 1.4°$ on the unprinted areas ($\theta_{g,r}$) (Figure 3.1C, the error bars are calculated from 3 different trials with 95% confidence). This significant difference in receding contact angles in the absence of particles in the droplet is hypothesized to be related to the differences in roughness in different regions. This is consistent with previous works that also saw significant reductions in receding contact angles at similar changes in roughness[31], [97].

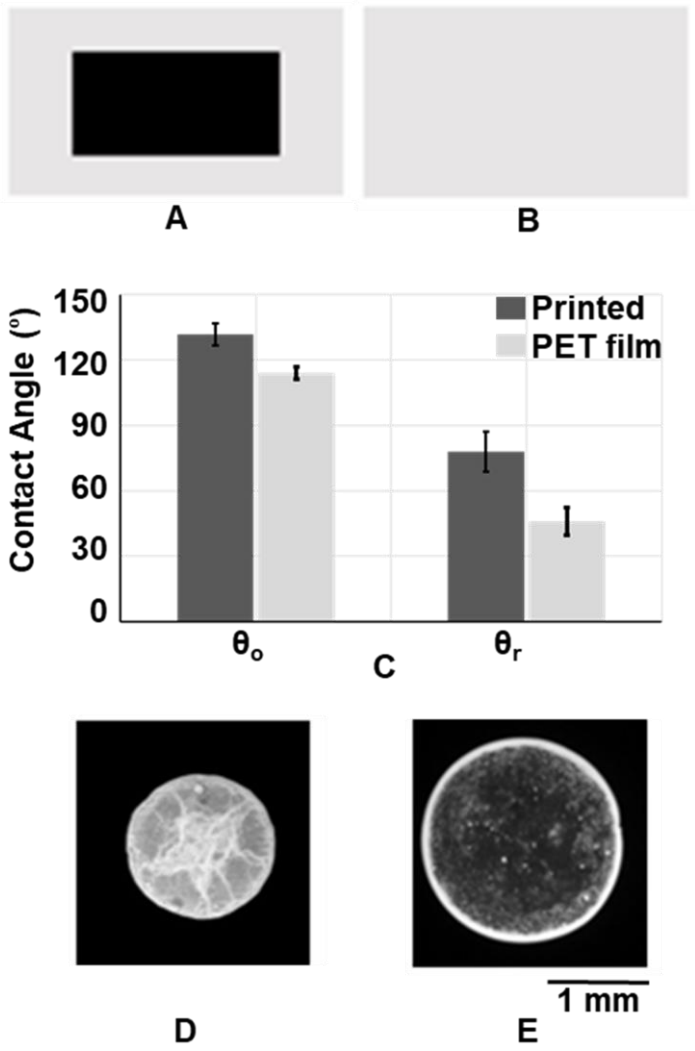

Figure 3.1: The top view of the control surfaces with a spin coated PDMS top layer on PET films (A) with and (B) without the printed layer. (C) The measured initial contact angle (left columns) and receding contact angles (right columns) for both control conditions are shown in (A) and (B). (D and E) Deposition patterns left by the evaporation of $0.02\ wt\%\ 1\ \mu m$ PS on PDMS coated control surfaces with and without printed layers.

Since receding contact angles can be impacted by the presence and properties of particles[84], experiments are performed to examine whether differences in wettability persisted in particle laden droplets on these surfaces.

The influence of the presence of particles on the contact line mobility on printed and non-printed devices is further characterized by examining deposition patterns left by evaporating particle-laden droplets ($0.02\ wt\%$ of $1\ \mu m$ PS particles) on homogeneous printed and non-printed surfaces (Figures 3.1A and 3.1B). A large ring-like pattern is observed on the non-printed device (Figure 3.1E). This is consistent with a deposition from a droplet with a low receding contact angle where droplet evaporation occurs mostly in the CCD mode. A smaller, more uniform pattern is observed on the printed device (Figure 3.1D). This is consistent with the expected deposition pattern for droplets that transition into the CCA mode due to relatively high receding contact angles.

The differences in both the receding contact angles and the resultant deposition patterns on printed and non-printed surfaces suggest hybrid dewetting may be possible on a surface with printed and non-printed regions. The hypothesis that heterogeneous dewetting can be achieved on these devices is tested by examining the effects of particle size, device geometry, and particle concentration on the transport and deposition of particles in evaporating droplets on these surfaces.

4 Understanding modes of evaporation on heterogeneous wettability surfaces

The goal of this chapter is to understand the deposition patterns on heterogeneous wettability surfaces. To do so, it is important to find out the contact line movement on heterogeneous wettability surfaces. By studying the fluorescent images, the scanning electron microscopy images, and the time-series images, differences in contact line mobility over the heterogeneous wettability surfaces are examined. After that, we proposed several evaporative modes to analyze the contact line movement over the heterogeneous wettability surfaces.

4.1 Fluorescent and SEM images

Our hypothesis is first tested by evaporating 3 μL droplets containing 0.02 $wt\%$ 6 μm PS particles on a device where $L_p = L_g = 100\ \mu m$. A relatively large particle diameter is chosen for these initial tests because previous investigations suggest that larger particles are less likely to affect contact line motion[24], [51]. Initial fluorescent images of

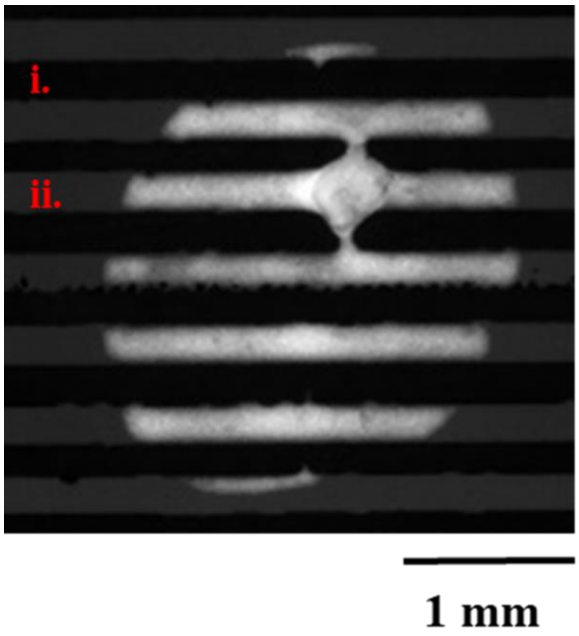

Figure 4.1: Fluorescent image of a deposition pattern with particle size 6 μm (0.2 $wt\%$). i) Printed region; ii) gap region.

deposition patterns suggest that particles self-assemble in the gaps between the printed regions (Figure 4.1). Here, the majority of the fluorescence intensity ($\overline{IG} = 0.90$) is observed above gap regions on the device, while a fraction of the fluorescence intensity ($\overline{IP} = 0.097$) is observed over printed regions.

Scanning electron microscopy (SEM) images of the same deposition pattern (Figure 4.2) confirm that particles are generally deposited above the gap regions, with very

little deposition on the printed regions. Higher magnification images (Figures 4.2C and 4.2D) showed that the edge of the printed regions creates a clear demarcation where particle deposition begins. While particle self-assembly is generally observed in the gap regions, particles do span the printed regions in one portion of the deposition pattern (see Figure 4.2B). This appears to be the result of mixed-mode deposition that occurs at the end of droplet evaporation where particles could not be transported away from the printed region prior to complete evaporation of the droplet.

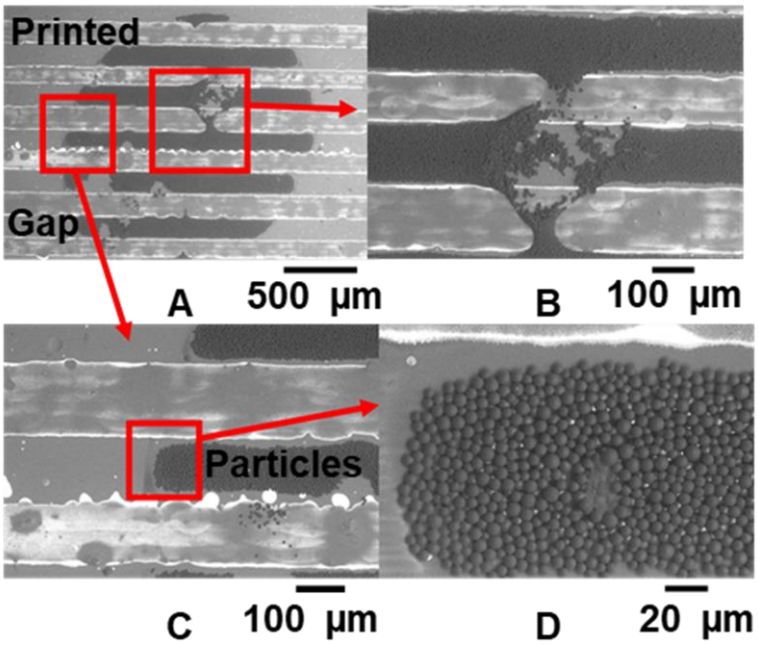

Figure 4.2: SEM images of a deposition pattern from a droplet seeded with 6 µm particles (0.02 *wt*%). The top left image (A) shows the whole deposition pattern and the remaining images (B-D) show zoomed in areas.

4.2 Time-series images

To further understand the non-uniform deposition patterns observed in Figures 4.1 and 4.2, top-view time-series images of the droplet during evaporation are examined (Figure 4.3). Images in Figure 4.3 are from a case with 1 μm PS particles at 0.02 $wt\%$

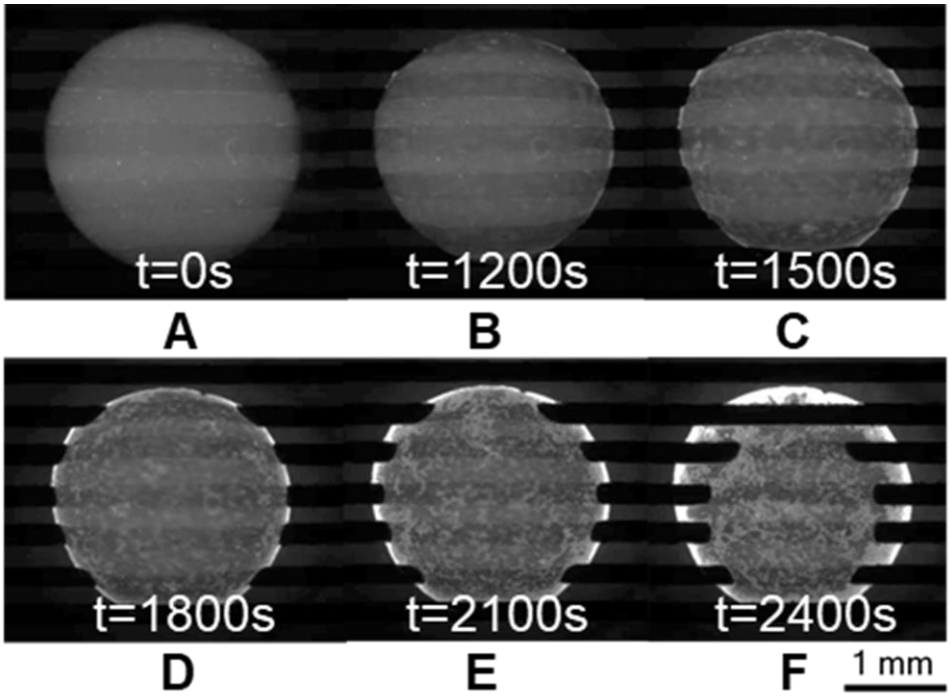

Figure 4.3: The time-series deposition patterns of the droplet containing 1 μm PS particles during evaporation on the PDMS devices (+50% contrast correction). The image is captured at the time $t = 0s$ to $t = 1000s$ for (A-F). The scale bar for all the images is the same and is shown at the bottom for (A-F).

concentration, but videos of all particle sizes and device geometries are available in the supplemental information (a list of supplemental videos can be found in the supporting information). Initially, the contact line of the droplet is approximately circular and evaporation appeared to proceed in the CCD mode (Figures 4.3A and 4.3B). Non-uniform contact line recession began between 1500 s (Figure 4.3C) and 1800 s (Figure 4.3D). Here, the contact line receded above printed regions but remained pinned over gap regions

(Figures 4.3D and 4.3E). This non-uniform recession of the contact line continued for the rest of the evaporation (Figure 8F).

4.3 Scalloped modes

Top-down videos of droplet evaporation in these experiments show that the advection of particles to the pinned portions of the contact line is an important mechanism for the transport of particles from above the printed regions to above the gap regions (supplemental videos). It seems as though this transport phenomenon is more prevalent above the gap regions where the contact line is pinned than above the printed region where the contact line is receding. Sketches depicting the evolution of the interface shape and observed modes of evaporation are presented in Figure 4.4.

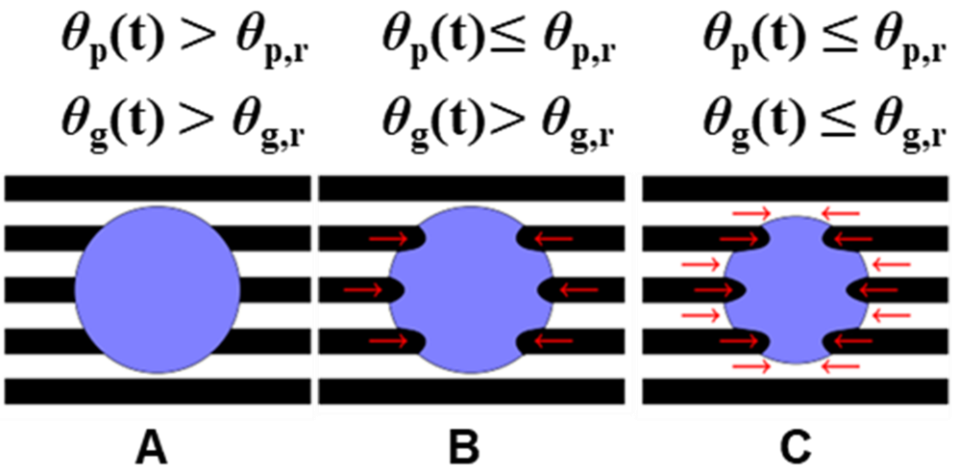

Figure 4.4: Top view illustration of the droplet during evaporation. The contact line may pin or move depending on the relationship between the local contact angles over the printed ($\theta_p(t)$) and gap ($\theta_g(t)$) regions and their associated receding contact angles ($\theta_{p,r}$ and $\theta_{p,r}$): (A) CCD, the contact line is pinned everywhere, $\theta_p(t) > \theta_{p,r}$ and $\theta_g(t) > \theta_{g,r}$; (B) scalloped-CCD, the contact line only recedes over the printed region, $\theta_p(t) \leq \theta_{p,r}$ and $\theta_g(t) > \theta_{g,r}$; and (C) scalloped-CCA, the contact line receded over both printed and gap regions $\theta_p(t) \leq \theta_{p,r}$ and $\theta_p(t) \leq \theta_{p,r}$.

A general conceptual model for the transition between these two modes can be provided by considering the difference between the local transient and receding contact

angles. When the local contact angle above the printed regions ($\theta_p(t)$) decreases to the receding contact angel above the printed regions ($\theta_{p,r}$), the portion of the contact line over these regions would be expected to recede. Similarly, the contact line above the gap regions would be expected to remain pinned while the local contact angle above those regions ($\theta_g(t)$) is above the receding angle for the gap regions ($\theta_{g,r}$). This model hypotheses that the non-uniform recession of the contact line led to a different series of evaporation modes such that: (1) CCD (Figure 9A) occurs when $\theta_g(t) > \theta_{g,r}$ and $\theta_p(t) > \theta_{p,r}$; (2) "scalloped-CCD" (Figure 9B) occurs where the contact line recedes over the printed regions (which are locally experiencing CCA), but not over the gap regions (CCD locally) ($\theta_g(t) > \theta_{g,r}$ and $\theta_p(t) \leq \theta_{p,r}$); and (3) "scalloped-CCA" (Figure 9C), where the entire contact line is receding but the scalloped shape is retained because the droplet passed through the scalloped-CCD mode ($\theta_g(t) \leq \theta_{g,r}$ and $\theta_p(t) \leq \theta_{p,r}$). Note that the scalloped-CCD and scalloped-CCA modes could include consistent or stick-slip recession of the contact line and the complexity of this model could be increased by including the contributions of effects of surface defects and particle effects on the local receding contact angles.

When the droplet is evaporating in the scalloped-CCD mode, advection to the contact line is expected to be strongest near the pinned portion of the contact line and particle diffusion should be more important away from the contact line, particularly above the printed region where advective velocities are expected to be lower[89]. As such, the local Péclet number (advection/diffusion) is expected to be higher near the pinned portion of the contact line and lower away from the pinned contact line (toward the apex of the

droplet and above the printed regions see supplemental videos). It is also expected that advective transport would act more strongly in the direction of the pinned portions of the contact line, and not radially outward as it would in an axisymmetric droplet on a homogeneous surface[50].

5-7 Effects on transport and deposition in evaporation droplets on surfaces with heterogeneous wettability

In these chapters, the influences of the heterogeneous wettability will be tested by examining deposition patterns left by particle-laden droplets evaporated on heterogeneous surfaces. In particular, we will examine the effects of particle size, device geometry (relative widths of L_g and L_p), and particle concentration.

For these chapters, we will examine the effects of particle size, device geometry, and particle concentration on the transport and deposition of particles in evaporating droplets on surfaces with heterogeneous wettability similar to that examined in Figures 4.1-4.4. A summary of the deposition patterns observed over the range of these parameters is shown in Figure 5.4.

The materials presented in this chapter have been published in *Langmuir*[98]. Reprinted with the permission from Xi Li, Kara L. Maki, and Michael J. Schertzer, Characterization of Particle Transport and Deposition Due to Heterogeneous Dewetting on Low-Cost Inkjet-Printed Devices. Langmuir 2023, Nov 14, https://doi-org.ezproxy.rit.edu/10.1021/acs.langmuir.3c02224.

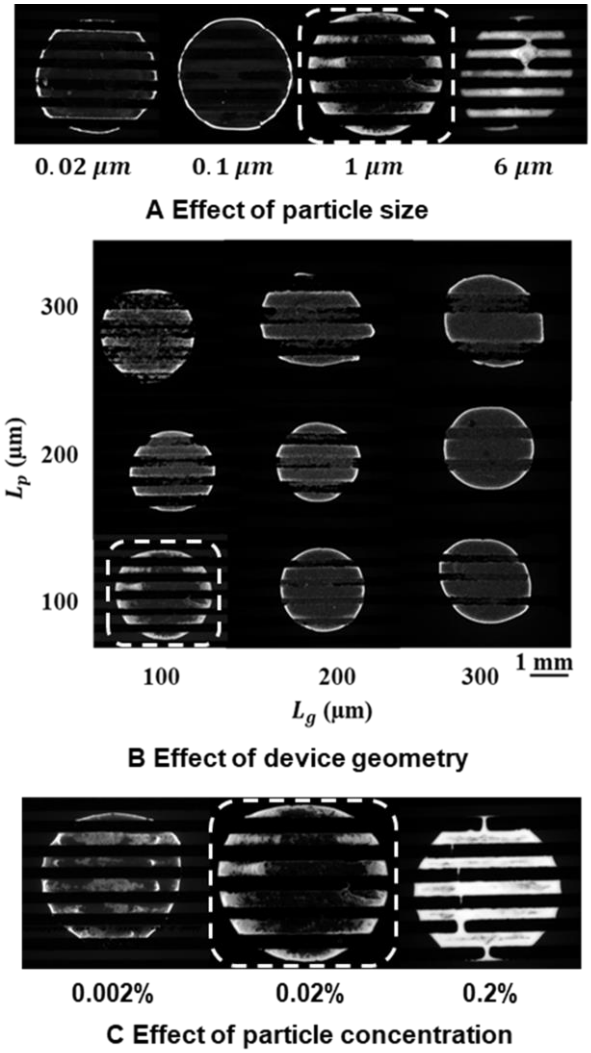

Figure 5.1: Deposition patterns left by evaporating 3 μL droplet on a variety of surfaces with heterogeneous wettability. (A) effect of particle size 0.02 to 6 μm; (B) effect of device geometry L_p and L_g between 100 μm and 300 μm; and (C) effect of particle concentration between 0.002 wt% to 0.2 wt%. The experimental case with particle size of 1 μm, $L_p = L_g = 100\ \mu m$, and particle concentration of 0.02% is consistent throughout each set of experiments and identified by the dashed border.

5 Effect of particle size on transport and deposition in evaporation droplets on surfaces with heterogeneous wettability

The goal of this chapter is to understand the interactions of particle size and heterogeneous wettability on the particle deposition. The hypothesis that the heterogeneous wettability could be influenced by the particle size is tested by changing the particle size between 0.02 μm and 6 μm. It is found that smaller particles trend to aggregate at the contact line while larger particles have some segments in the middle.

The effect of particle size on deposition patterns left by evaporating droplets is tested by examining deposition patterns left by droplets containing particles with diameters between 0.02 μm and 6 μm (Figure 5.2). Particle concentration in all cases is held constant at $0.02\ wt\%$, and L_g and L_p are both held constant at $100\ \mu m$. The vast majority of particle deposition is observed to be over the gap regions for all particle sizes examined here. The average grayscale intensity ($\overline{IG}$, eq 6) across the entire gap region is greater than 0.76 for all particle sizes (Figure 5.2E, the error bars are calculated from 3 different trials with 95% confidence). Fluorescence intensity above the gap region increased from 0.77 to 0.98 as particle size increased from $0.02\ \mu m$ to $1.0\ \mu m$. It then falls to 0.90 as the particle size is further increased to $6\ \mu m$. The reduction in fluorescence intensity above the gap region in the $6\ \mu m$ case is due to a circular deposition near the center of the pattern that appears to have been deposited as the receding contact lines on multiple printed regions met and particles are unable to migrate to the adjacent printed region prior to deposition (Figure 5.2D).

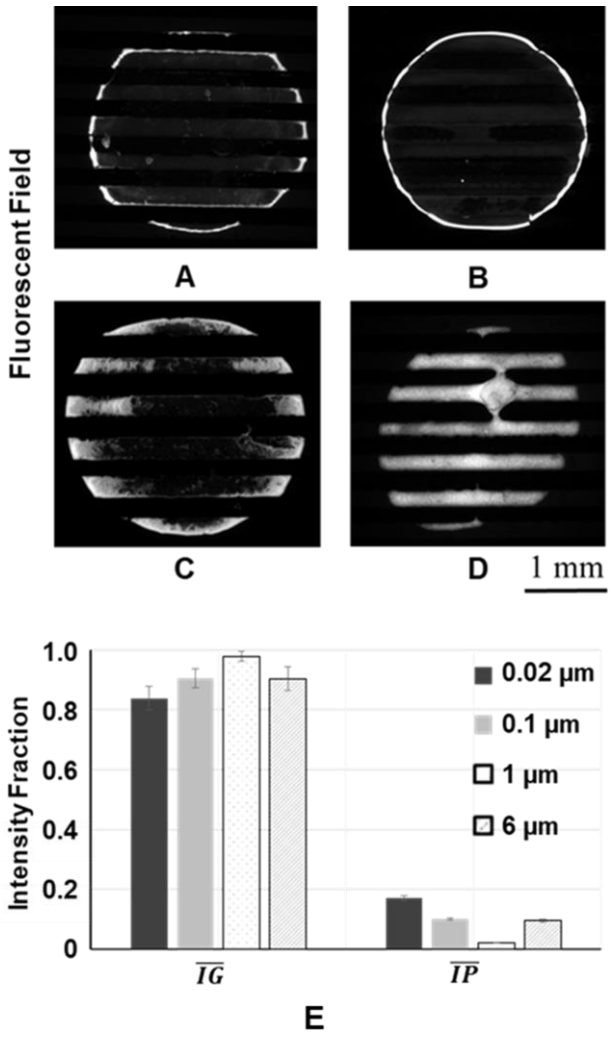

Figure 5.2: Colloidal deposition patterns of 3 μL droplet with different PS particles size from 0.02 to 6 μm. (A-D) The raw images in the fluorescent field. (E) The average distribution of intensity fraction in eq 6 analysis data with different PS particles size: 0.02μm (solid dark), 0.1μm (solid grey), 1μm (dots), and6 μm (stripped).

While the vast majority of the fluorescence intensity is observed above the gap regions for the deposition patterns for all particle sizes examined here (Figure 5.2E), the distribution of the fluorescence intensity within the gap regions changed with particle size (Figure 5.2). Deposition patterns from the smallest particles examined here (0.02 μm and 0.1 μm) left segmented ring deposition patterns where most of the fluorescence intensity, $\bar{I}_k$ for $k \in \{1, 2, 3, 4, 37, 38, 39, 40\}$ in eq 5, is observed at the position of the initial contact line (Figure 5.3). As particle size increased to 1 μm and then 6 μm, deposition mainly occurred on the gap region, but fluorescence intensity in the center of the deposition pattern, $\bar{I}_k$ for $k = 5, \ldots, 35$ in eq 5, increased with particle size (Figures 5.3).

Diameter (μm)	u_i	$\dot{x}_p$
0.02	0.73	5.2
0.1	0.64	2.3
1	0.54	0.7
6	0.50	0.3

Table 5.1: Interface velocity (u_i), and diffusion rate ($\dot{x}_p$) as a function of particle diameter.

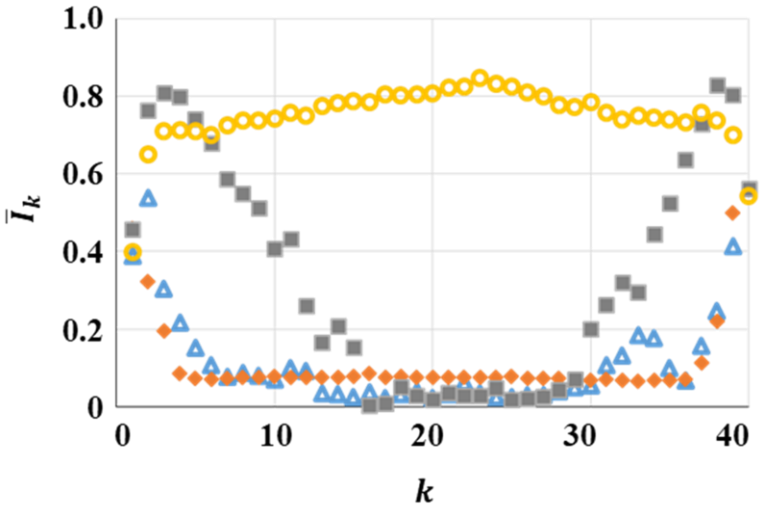

Figure 5.3: Averaged horizontal distribution of intensity fraction eq 5 of colloidal deposition patterns of 3 µl droplet with different PS particles size from 0.02 to 6 μm. The intensity is split into 40 sections based on the whole strips: 0.02 μm (orange diamond), 0.1 μm (blue triangle), 1 μm (grey rectangle), and 6 μm (yellow circle).

The change in the spatial distribution of fluorescence intensity above the gap regions as a function of particle size is consistent with expectations for the transition between the importance of the descending interface velocity (u_i) and particle diffusion rate ($\dot{x}_p$) (Figure 5.4, Table 5.1). As described in previous works[62], [94], when $u_i > \dot{x}_p$, particles tend to be captured on the descending interface and deposited uniformly and not in a ring at the contact line. This case is observed for the 6 μm diameter particle, which had the slowest particle diffusion rate examined here. As particle size is reduced to 1 μm, $\dot{x}_p$ and u_i are of similar magnitude and a transitional pattern is observed. As particle size is reduced below 1 μm, $\dot{x}_p$ is appreciably larger than u_i and particles escape the descending interface to be advected to the contact line and deposited as a segmented ring. While the behaviors of interface capture are present here, the mechanisms that transport particles from above the printed regions to above the gap regions appeared to remain robust.

Summary

The investigation tests the heterogeneous wettability by the particle size between 0.02 μm and 6 μm. It demonstrates that more particles would be deposited over the gap region when the particle size increased from 0.02 μm, 0.1 μm to 1 μm. Moreover, more particles are deposited towards the center when the particle size increased. By comparing the descending interface velocity and particle diffusion rate, the particle size would be the key factor in influencing the deposition regions over the heterogeneous wettability surfaces. This point is also close to the previous studies[77].

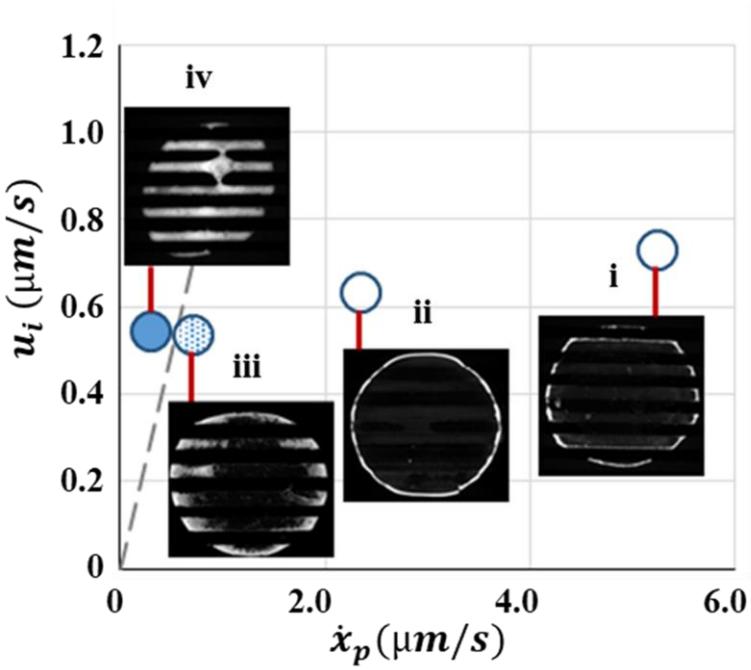

Figure 5.4: Phase diagram for particle deposition as a function of the velocity of the descending interface (u_i) and the particle diffusion rate ($\dot{x}_p$). Images of the resulting deposition for each particle size are shown inset: i) 0.02 μm, ii) 0.1 μm, iii) 1 μm, iv) 6 μm. Dash line indicates that u_i is equal to $\dot{x}_p$.

6 Effect of printed geometry on transport and deposition in evaporation droplets on surfaces with heterogeneous wettability

The goal of this chapter is to test the heterogeneous wettability under the influences of printed geometry. The hypothesis is that the heterogeneous wettability could be influenced by changing the width of the striped patterns and gaps. It is found that the particle concentration gradient between the gap and printed regions could influence the heterogeneous wettability during evaporation.

The effect of device geometry on patterns left by evaporating droplets is examined by varying L_p and L_g widths between $100\,\mu m$ and $300\,\mu m$ (Figure 6.1). These experiments are performed using 3 μL droplets with $0.02\,wt\%$ of 1 μm PS particles where interface capture and particle diffusion are approximately equal. The fraction of fluorescence intensity observed over the gap regions ($\overline{IG}$) is measured in each case (Table 6.1, the error bars are calculated from 3 different trials with 95% confidence).

L_p(μm)	L_g(μm)		
	100	200	300
300	0.47±0.04	0.50±0.03	0.65±0.05
200	0.52±0.04	0.54±0.03	0.76±0.04
100	0.98±0.01	0.65±0.04	0.82±0.05

Table 6.1: The intensity fraction distributions over the gap regions ($\overline{IG}$) as a function of device geometry.

The $\overline{IG}$ data in Table 6.1 suggest that radial transport to the contact line is important for the separation of particles between the gap and printed regions. For all values of L_g, $\overline{IG}$ increased as L_p decreased. As L_p decreased, less of the contact line is receding and more of the contact line is pinned. In this case, advection seems more likely to carry any given particle to the pinned parts of the contact line. A reduction in L_p would also reduce the distance required for a particle to be transported out of a printed region and into a gap region where advection to the contact line is likely stronger.

The direct relationship between L_g and $\overline{IG}$ for a given value of L_p is less clear. For the larger values of L_p (200 μm and 300 μm), $\overline{IG}$ increased with L_g. But at the smallest value of L_p (100 μm), the trend is non-monotonic with $\overline{IG}$ first falling as L_g is increased from 100 μm to 200 μm, before increasing as L_g is increased from 300 μm. This suggests that the interplay between these variables may be more complex.

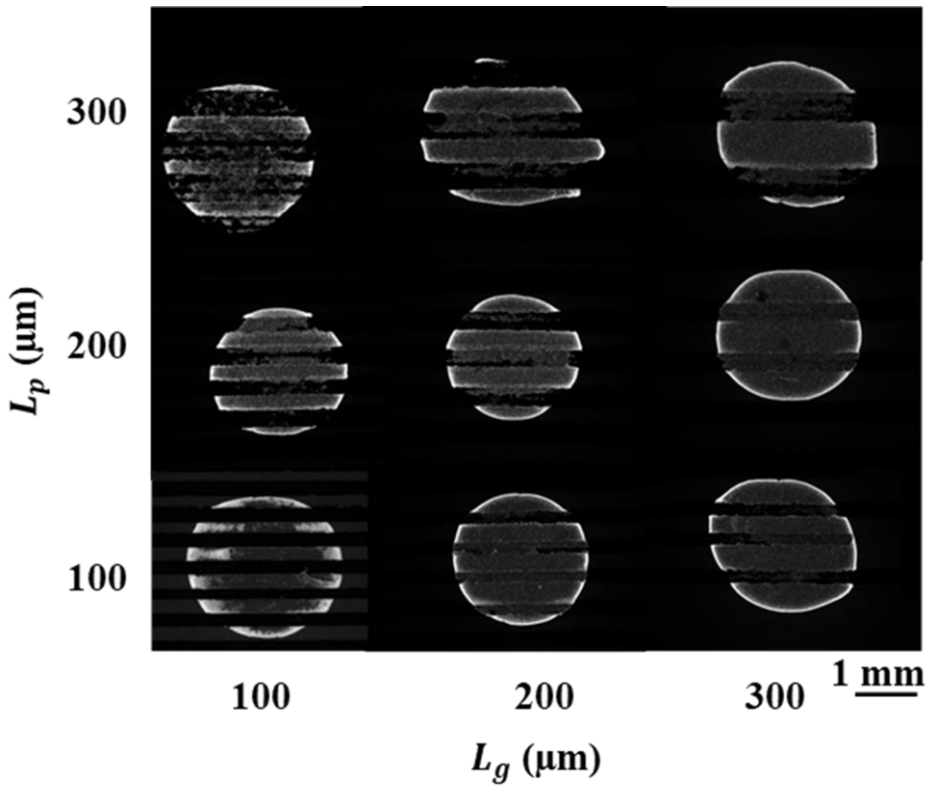

Figure 6.1: Fluorescent field deposition images of the 3 μL droplet with 0.02 $wt\%$ 1 μm PS particles after evaporation. From left to right, the gap width (L_g) increases from 100 μm to 300 μm. From bottom to top, the printed width (L_p) increases from 100 μm to 300 μm.

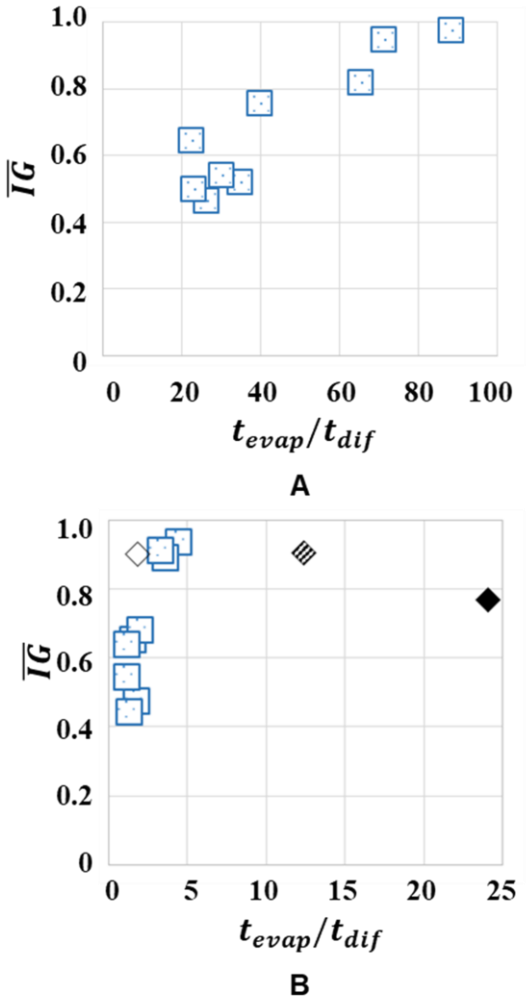

Figure 6.2: Fraction of fluorescence intensity observed over the gap region as a function of the ratio of characteristic times for advection to the pinned contact line and diffusion across the printed region for cases examining (A) device geometry with particle diameter of 1 μm (open square) and (B) device geometry (open square) and those where $L_p = L_g = 100\,\mu m$ with particles sizes of $6\,\mu m$ (open diamond), $0.1\,\mu m$ (hashed diamond) and $0.02\,\mu m$ (filled diamond).

To better understand particle transport from above a printed region to adjacent gap regions, the effects of the ratio of evaporation time to a characteristic diffusion time for particles to cross the printed region ($t_{dif} = \dot{x}_p/L_p$) on $\overline{IG}$ is studied (Figure 6.2A). This provided a reasonable collapse of the data, with a linear coefficient of determination (r^2) of 0.84 and a slope of 0.037 ± 0.012 (95% confidence interval). Physically, this suggests

that the effectiveness of particle transport from the above printed regions to above the gap regions improved when particles above the printed regions had more time to diffuse toward the gap regions where they are transported to the pinned portion of the contact line by advection.

While the trials used to specifically examine device geometry collapsed fairly well in Figure 6.2A open squared, the collapse of the data is not complete when trials used to examine the effects of particle size are included (Figure 6.2B the squares and diamonds). The $6\,um$ particle data fit the trend observed in Figure 6.2B, but the smaller particles ($0.1\,\mu m$ and $0.02\,\mu m$) did not. Interestingly, the deposition pattern left by the $6\,um$ particles also more closely resembled those seen for the $1\,\mu m$ cases than do those left by the $0.1\,\mu m$ and $0.02\,\mu m$ particles (see Figures 5.1-5.3). One potential reason for the lack of collapse at small particle sizes could be that the recession of the contact line appeared to begin later in the small particle cases. This may be due to the ability of smaller particles to get closer to the contact line and delay depinning[24]. The delayed recession of the contact line above the printed region would promote a more uniform advection to the contact line. This would keep particle concentration above the gap and printed regions relatively equal so the net diffusion of particles from above the printed regions to above the gap regions would be slowed despite the higher characteristic diffusion speed expected from the smaller particles.

Summary

The investigation tests the heterogeneous wettability based on the printed geometry. Different widths of the gap and printed regions have been studied from $100\ \mu m$ to $300\ \mu m$. It demonstrates that more particles would be deposited over the gap region when the L_g increased or L_p decreased. More advection to the contact line would be expected to influence the deposition patterns in these cases. Moreover, the different physical distance for the particles to move between the gap region and the printed region may be another key point. Last, the instant particle concentration gradient between the gap region and the printed region may lead to the differences.

7 Effect of particle concentration on transport and deposition in evaporation droplets on surfaces with heterogeneous wettability

The goal of this chapter is to test the heterogeneous wettability under the influences of the particle concentrations. The hypothesis is that the heterogeneous wettability could be influenced by changing the concentration of the particles. It is found that the uniformity of the depositions increased with the concentration.

The effect of particle concentration on the transport and deposition of particles in droplets evaporated on heterogeneous surfaces is tested by examining the concentration (g/ml) of 1 μm PS particles at $0.002\ wt\%$, $0.02\ wt\%$, and $0.2\ wt\%$. These experiments are performed on devices where $L_p = L_g = 100\ \mu m$. Fluorescence intensity is again predominantly located over the gap regions with approximately $\overline{IG}$ ≈0.95, 0.98, and 0.92 for $0.002\ wt\%$, $0.02\ wt\%$, and $0.2\ wt\%$, respectively (Figure 7.1D, the error bars are calculated from 3 different trials with 95% confidence). The decreased fluorescence intensity above the gap regions in the $0.2\ wt\%$ case suggests that there may be some limit to the capacity for the deposition of particles in the gap regions. After this capacity is reached, particles appear to be deposited above the printed regions. The shape of the deposition above the printed regions in Figure 7.1C suggests that deposition occurs as opposing receding contact lines above the same printed region meet and particles are unable to migrate to a gap region before being deposited. Recall a similar trend is observed in Figure 5.3 when comparing the percentage of particles deposited in the gap regions for larger sized particles to smaller sized particles.

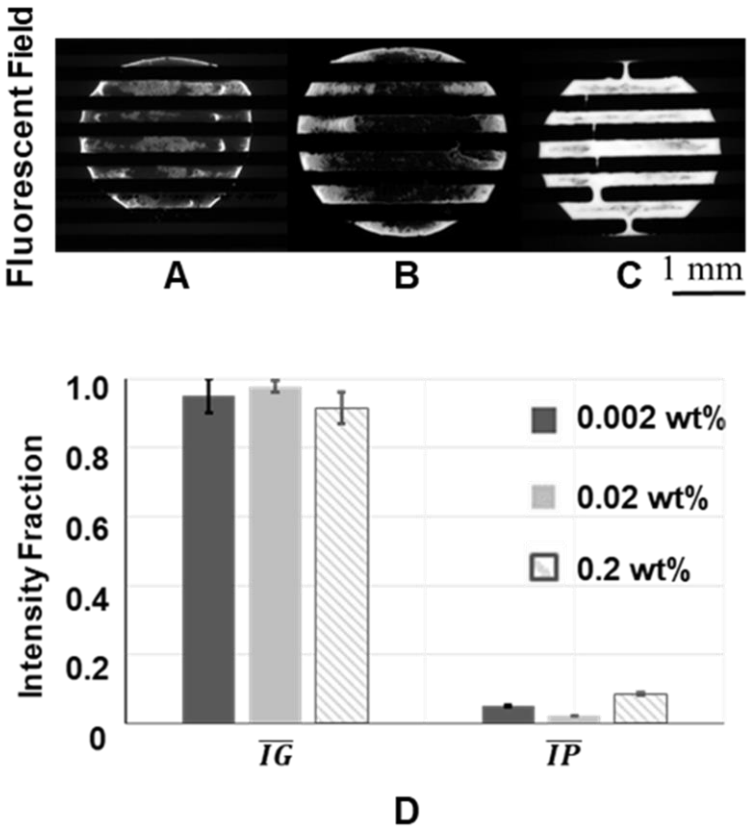

Figure 7.1: Colloidal deposition patterns of 3 μL droplet with 1 μm PS particles with different concentrations of (A) 0.002 wt%, (B) 0.02 wt%, and (C) 0.2 wt%. (D) The average distribution of intensity fraction in eq 5 analysis data with different concentrations: 0.002 wt% (solid dark), 0.02 wt% (solid grey), and 0.2 wt% (stripped).

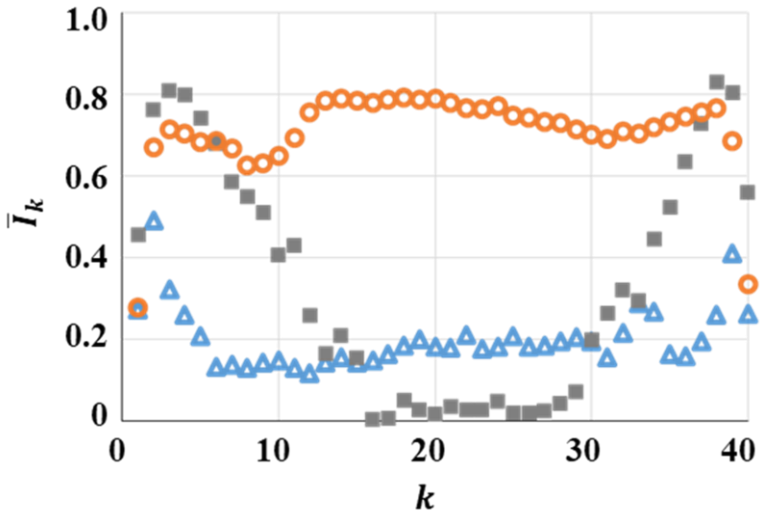

Figure 7.2: The gray fraction percentage of colloidal deposition patterns of 3 μl droplet with different PS particles concentration from 0.002 wt% to 0.2 wt%. The intensity is split into 40 sections based on the whole strips: 0.002 wt% (blue triangle), 0.02 wt% (grey rectangle), and 0.2 wt% (orange circle).

As particle concentration increased, fluorescence intensity over the gap regions, $\bar{I}_k$ for $k = 1, \ldots, 40$ in eq 5, became more uniformly distributed (Figure 7.2). Segmented-ring depositions are observed at the smallest concentration $0.002\ wt\%$, (Figure 7.2). But as particle concentration increased to $0.02\ wt\%$ and $0.2\ wt\%$, the fluorescence intensity toward the center of the gap regions increased, until it is relatively uniform in the $0.2\ wt\%$ cases (Figure 7.2). The transition from ring-like to more uniform deposition patterns observed here is similar to that seen on homogeneous surfaces[50], [69], [70], [99], [100]. The transition from ring-like depositions to more uniform depositions with increasing concentration has often been attributed to an increase in slip-stick behavior at higher concentrations that leads to the deposition of a large number of concentric rings during evaporation[24], [50], [77], [83].

Summary

The investigation tests the heterogeneous wettability with different particle concentrations. Different particle concentrations have been studied from $0.002\ wt\%$, $0.02\ wt\%$, to $0.2\ wt\%$. More particles would be expected to deposit over the gap region with higher concentrations. This phenomenon is similar to the cases over homogeneous surfaces. However, when the concentration is too high like $0.2\ wt\%$, some particles may be pushed to the printed region as too tiny spaces.

8 Future works

The goal of this chapter is to generate some new ideas and preliminary tests over the heterogeneous wettability surfaces. The first idea is to test multiple other shapes or geometry fabricated surfaces. The studies in the previous chapters mostly focus on the contact line hysteresis over horizontal and vertical directions. We would like to find out whether the radial and other directions follow similar rules as previous studies. Moreover, with the electrowetting method, the contact line would be easier to move. So, it would be interesting to study the heterogeneous wettability behavior with the electrowetting method.

8.1 Effect of Pie shape geometry on transport and deposition in evaporation droplets on surfaces with heterogeneous wettability

From the previous experiments, the design of the patterns is mostly based on the strip patterns which are parallel rectangles. If the droplets had sphere caps over the homogeneous surfaces in the ideal situation, they would recede homogenous in the radial direction. Previous experiments showed the contact line has different receding behaviors over the strip patterns. However, within the rectangle strips, the contact line might also recede differently in horizontal or vertical directions due to the different lengths and widths of the rectangles. So, the studies of the heterogeneous dewetting in radial direction would be interesting as future works.

The patterns are designed in Figure 8.1. The two printed regions are both quarter circles and the same as the gap regions. The same processes are used to fabricate the

quarter pi devices as strip pattern devices. The same droplet and particle concentration (contained $1\,\mu m$ and $6\,\mu m$ diameter fluorescent polystyrene particles $0.02\,wt\%$ in deionized (DI) water) are used as previous experiments for deposition in Figure 8.1.

In Figure 8.1, the deposition patterns of $1\,\mu m$ and $6\,\mu m$ PS particles could be seen in the Pie shape devices. In both cases, the contact line is pinned over the gap region with most particles left. This kind of contact line hysteresis is the same as we proposed in the strip patterns. For $1\,\mu m$ particles, there are still some left in the gap region while there are very few for $6\,\mu m$ particles. This is also similar to the trip pattern depositions. Interestingly, the $1\,\mu m$ particle deposition pattern in Figure 8.1 shows some particles left in the vertical direction over the printed region. This vertical direction is also the direction the contact line receded over the printed region. We then zoomed in with the printed patterns in Figure 8.2. In the red box, we could see the printer printed in the vertical direction. In this case, the contact line receded along the printed direction over the printed region rather than the radial direction. As a low-cost technique, the limitation of the printer may lead to the receding direction along the printing direction over the printed region. For future works, rotating the printed patterns at 45° or other degrees to test the influences of the printed direction on the heterogeneous surfaces.

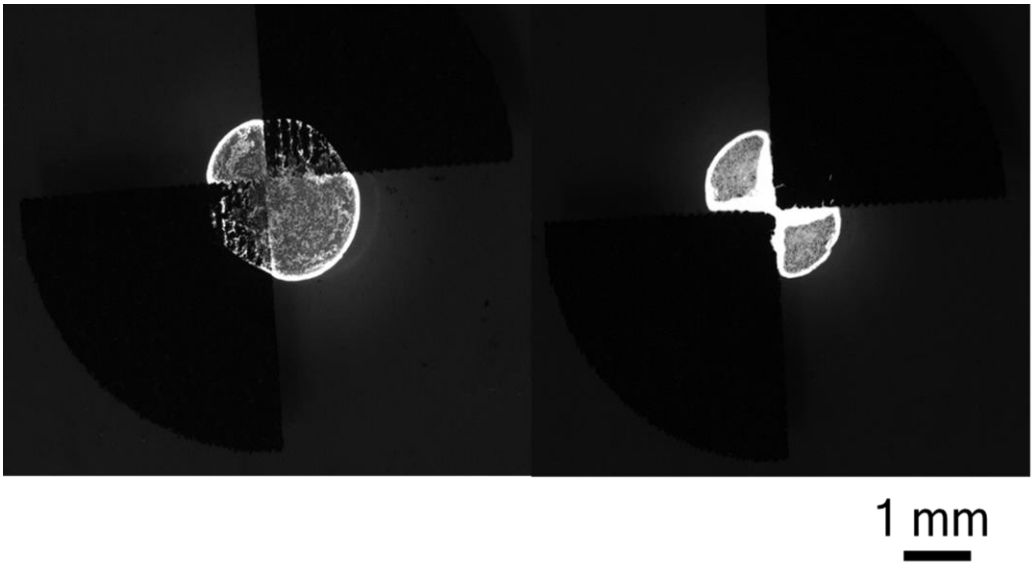

Figure 8.1: $1\ \mu m$ and $6\ \mu m$ deposition patterns on the Pie shape devices.

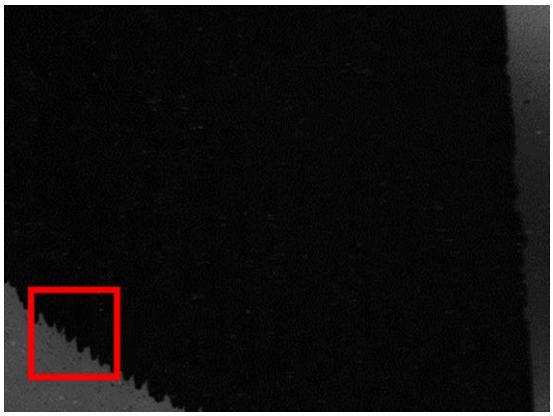

Figure 8.2: The zoom image of the Pie shape devices. The red box shows the printed direction.

8.2 Electrowetting

The electrowetting (EW) with electrophoresis (EP) technique has drawn significant attention in recent years[101]. With an applied voltage, this method provides an opportunity to control or modify the droplet and particles[102]. Different EW techniques have been studied to explain the motion of the particles with the DC field[103], [104].

In a DC field, the electro kinetic force will drive the charged particles toward the opposite charged electrodes[26]. The force that influences the charged particles under the uniform electric field is called the EP force is shown in figure 9A. EP effect has been studied for colloidal deposition for years. Jason et al. tried to separate TiO_2 particles with EP force for solar cell applications[105]. Other studies have shown the deposition can be controlled by the time and size of the partten column[106], [107]. EP effect has contributed to many rapidly growing fields, such as liquid lenses, biomedical diagnostics, and lab-on-a-chip systems, and become the most popular in microfluidics[108]–[111]. All the previous studies show the EP force is important for colloidal deposition.

Orejon et al. hypothesized EP manipulation could dominate the capillary flows, hydrothermal flows, and oscillatory movement of the contact line[26]. They found that deposition patterns left by TiO_2 in evaporating water droplets on amorphous fluoropolymer substrates are more uniform. In the hypothesis, the EP force would govern the contact line motion and internal flow during evaporation by influencing the particles. Therefore, it would be possible to predict the deposition of the particles after drying.

Orejon et al. also established a model to predict the terminal EP velocity during evaporation. In the vertical direction, the force of the particles from the electric field $F_e = q * E$, where q is the charge of the particle and E is the electric field inside the droplet, will be balanced with Strokes-type viscous force, $F_S = 6\pi\eta r_p v_{ep}$, where η is the viscosity of the liquid, and r_p is the radius of the particle[26]. The electric field can be approximated by $E \approx V/h$, where V is the applied DC voltage and h is the height of the droplet. So we can derive the electrophoresis velocity from the balance:

$$v_{ep} = \frac{qV}{6\pi h\eta r} \tag{7}$$

Therefore, the electrophoresis force could be predicted and compared with different velocities during evaporation.

The hypothesis generated by Orejon et al[64] requires that charged particles within a droplet actuated with a DC potential experience attraction from the EP effect. Unfortunately, multiphysics models that simulate the electric field in DC actuated droplets in EW platforms suggest that no electric field could penetrate the dielectric layer under the DC voltage. In an effort to test the hypothesis generated by Orejon et al., we set out to repeat the previous numerical and experimental works. In addition to the experimental work done by Orejon et al., we also included the experimental case where both attractive and repulsive EP force could apply. We believe that this additional case tests the hypothesis of EP manipulation of particles in evaporating droplets under DC EW.

8.2.1 Numerical simulation

It could be doubted that the DC source Orejon et al. use may not be enough to penetrate the dielectric layer and the droplet. It indicates that there may be almost no electric field inside the droplet to provide the EP force. With the ground needle inside the droplet, the electrokinetic force may only influence the needle area and not the substrate. Lee et al. showed almost no electrical penetration inside the droplet with DC voltage[112]. Hong et al. simulated the electrical filed contour plot with different frequencies [113]. The plots suggest that no penetration even at 1 kHz frequency. The electric field did not penetrate the dielectric layer under the droplet at low frequency. While in the DC field, it is even harder to penetrate compared to the AC field. In this case, it is almost impossible to move particles with EP force. Studied need to continue on deposition under EP force as many aspects are still poorly understood.

From the hypothesis, no electric field could penetrate the dielectric layer under the DC voltage. If there is no electric field during evaporation, there should also be no EP forces. The droplets with particles will be set directly over the electrodes shown in figure 8.3A. A 2D symmetric COMSOL model has been set up to study the voltage penetration inside the droplet shown in figure 8.3. The input voltage is 18 V which is the same as Orejon's work. The voltage contour plot shows minimal penetrations inside the droplet. Therefore, EP force is expected to play an essential role during the evaporation. Those experiments without the dielectric layer would test the hypothesis of the EP force.

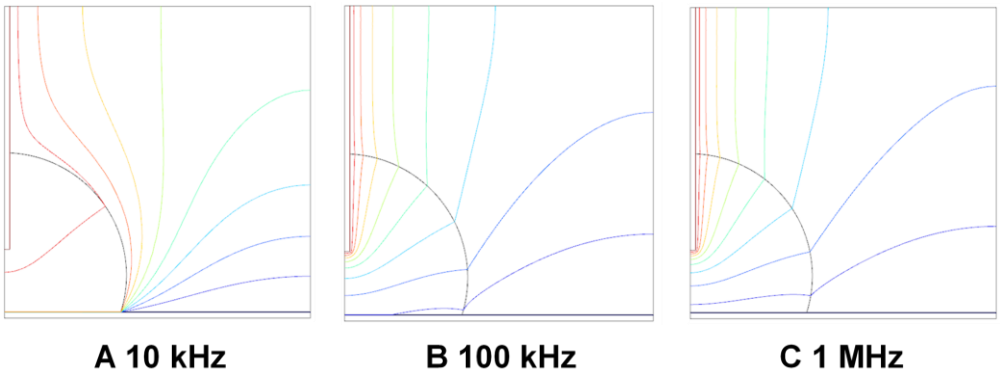

Figure 8.3: COMSOL simulation of the electric field around the droplets. The setup of the simulation are the same following Lee et al and Hong et al. The input voltage for all cases are 18 V with a needle inserted into the droplet in the center. The frequencies are (A) 10 kHz, (B) 100 kHz, and (C) 1 MHz.

8.2.2 Experiment results of electrowetting

Orejon et al proposed that the attractive EP force could pull the particles down to the surfaces faster than other forces during evaporation. They did observe more uniform deposition under the DC voltage compared with no voltage. However, if their hypothesis could predict the attractive cases, what would happen when we flip the electrodes and keep the rest setup the same? From their hypothesis, the repulsive particles would be pushed away from the surfaces to reduce the contact line pinning forces. Therefore, the final deposition pattern would be a much smaller ring compared to attractive cases. Orejon et al did not test the reversed polarity of the electrode case. Also, from the simulation in Figure 8.3, we predict there is no EP forces in the DC cases. It would be worthy to repeat the Orejon et al's works with both attractive and repulsive cases to determine which hypothesis is not correct.

With the help of Akshay Pratap Singh, we did repeat the Orejon's work with the same setup. We also reversed the polarity of the electrodes and kept the rest of the setup the same to test their hypothesis. The deposition patterns of the attractive, repulsive, and control cases are shown in Figure 8.4. Compared with the control case at the top, we did see larger and more uniform patterns. However, there are no significant differences between the attractive and repulsive cases (middle and bottom). They are both bigger and uniform circles compared with the control case. This kind of similarity did not support the Orejon's hypothesis. From their hypothesis, the attractive and repulsive cases should be different as the particles are manipulated by the reverse EP forces. The repulsive particles

would be pushed away to form smaller deposition patterns while the attractive case should be larger patterns. Therefore, with both simulation and experiment data, there should be no EP forces during evaporation in the DC field.

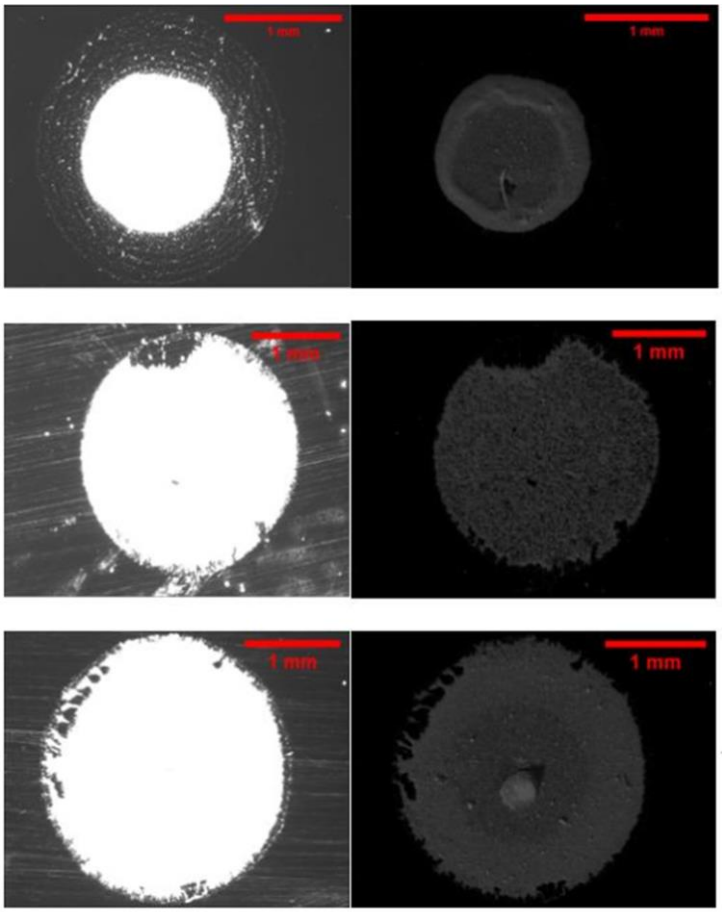

Figure 8.4: Deposition patterns of 0.05 wt% TiO_2 particles on SU-8 devices. Unactuated case(top), attractive DC (middle), and repulsive DC (bottom). Co-worked with Akshay Pratap Singh.

9 Conclusions

This investigation experimentally demonstrates robust particle self-assembly of polystyrene particles on surfaces with heterogeneous wettability created using relatively low-cost inkjet-printed fabrication techniques. Self-assembly is observed across a variety of particle sizes, concentrations, and device geometries.

Devices with heterogeneous wettability are fabricated by inkjet printing patterns on a flexible substrate prior to coating with a thin layer of PDMS. While initial contact angles on these surfaces are similar, the receding contact angles above the printed regions are significantly higher than those over non-printed or gap regions. This difference in receding contact angles gave rise to a "scalloped" contact line shape during evaporation as the contact line receded over the printed areas, but remained pinned over the gaps.

While the heterogeneous wettability of the surfaces examined here provided a fairly robust separation of particles between printed and gap regions, mechanisms that governed particle distribution within the deposition are similar to those seen in evaporating droplets on homogeneous surfaces. Experiments examining the effects of particle size on depositions on these surfaces showed that smaller particles are more likely to deposit near the contact line in the gap regions where larger particles are more uniformly distributed. This is consistent with the competition between the advective flow to the contact line and interface trapping that has been observed on homogeneous surfaces.

In general, particle separation between the printed and gap regions on the heterogeneous surface is improved when gap regions are larger and printed regions are smaller. We hypothesized that (i) advection to the contact line governs transport near the pinned contact line of the gap regions and (ii) particle diffusion governs transport over the gap regions. When a larger fraction of the contact line is pinned, the advective flow to the contact line is more effective at bringing particles to the pinned portion of the contact line. But as the width of the printed regions increased, particles in that region took more time to diffuse to the gap regions where the advective flow would bring them to the pinned portion of the contact line.

Experiments here also observed that increasing particle concentration tended to result in more uniform depositions on the gap regions of the device. This has also been previously seen on homogeneous surfaces that the transition from ring-like depositions to more uniform depositions with increasing concentration due to an increase in slip-stick behavior at higher concentrations.

Reference

[1] M. Edalatpour, L. Liu, A. M. Jacobi, K. F. Eid, and A. D. Sommers, "Managing water on heat transfer surfaces: A critical review of techniques to modify surface wettability for applications with condensation or evaporation," *Applied Energy*, vol. 222, pp. 967–992, Jul. 2018, doi: 10.1016/j.apenergy.2018.03.178.

[2] D. Seo, J. Lee, C. Lee, and Y. Nam, "The effects of surface wettability on the fog and dew moisture harvesting performance on tubular surfaces," *Sci Rep*, vol. 6, p. 24276, Apr. 2016, doi: 10.1038/srep24276.

[3] B. M. Weon and J. H. Je, "Fingering inside the coffee ring," *Phys. Rev. E*, vol. 87, no. 1, p. 013003, Jan. 2013, doi: 10.1103/PhysRevE.87.013003.

[4] K. S. A. *et al.*, "Super-hydrophobicity: Mechanism, fabrication and its application in medical implants to prevent biomaterial associated infections," *Journal of Industrial and Engineering Chemistry*, vol. 92, pp. 1–17, Dec. 2020, doi: 10.1016/j.jiec.2020.08.008.

[5] T. Yan *et al.*, "A magnetic pH-induced textile fabric with switchable wettability for intelligent oil/water separation," *Chemical Engineering Journal*, vol. 347, pp. 52–63, Sep. 2018, doi: 10.1016/j.cej.2018.04.021.

[6] X. Yue, T. Zhang, D. Yang, F. Qiu, Y. zhu, and J. Fang, "In situ fabrication dynamic carbon fabrics membrane with tunable wettability for selective oil–water separation," *Journal of Industrial and Engineering Chemistry*, vol. 61, pp. 188–196, May 2018, doi: 10.1016/j.jiec.2017.12.016.

[7] D. Tian, Y. Song, and L. Jiang, "Patterning of controllable surface wettability for printing techniques," *Chemical Society Reviews*, vol. 42, no. 12, pp. 5184–5209, 2013, doi: 10.1039/C3CS35501B.

[8] S. Ferraris and S. Spriano, "Antibacterial titanium surfaces for medical implants," *Materials Science and Engineering: C*, vol. 61, pp. 965–978, Apr. 2016, doi: 10.1016/j.msec.2015.12.062.

[9] F. Rupp *et al.*, "A review on the wettability of dental implant surfaces I: Theoretical and experimental aspects," *Acta Biomaterialia*, vol. 10, no. 7, pp. 2894–2906, Jul. 2014, doi: 10.1016/j.actbio.2014.02.040.

[10] C. G. Jothi Prakash and R. Prasanth, "Approaches to design a surface with tunable wettability: a review on surface properties," *J Mater Sci*, vol. 56, no. 1, pp. 108–135, Jan. 2021, doi: 10.1007/s10853-020-05116-1.

[11] X. Liu *et al.*, "Spontaneous Patterning of High-Resolution Electronics via Parallel Vacuum Ultraviolet," *Advanced Materials*, vol. 28, no. 31, pp. 6568–6573, 2016, doi: 10.1002/adma.201506151.

[12] W. Zhao *et al.*, "A Facile Method for the Growth of Organic Semiconductor Single Crystal Arrays on Polymer Dielectric toward Flexible Field-Effect Transistors," *Advanced Functional Materials*, vol. 29, no. 32, p. 1902494, 2019, doi: 10.1002/adfm.201902494.

[13] N. Bodin-Thomazo, F. Malloggi, and P. Guenoun, "Marker patterning: a spatially resolved method for tuning the wettability of PDMS," *RSC Advances*, vol. 7, no. 73, pp. 46514–46519, 2017, doi: 10.1039/C7RA05654K.

[14] M. He, Y. Yang, M. Mei, and H. Qiu, "Droplet Evaporation Dynamics on Hydrophobic Network Surfaces," *Langmuir*, vol. 38, no. 20, pp. 6395–6403, May 2022, doi: 10.1021/acs.langmuir.2c00479.

[15] J. Sun, B. Bao, J. Jiang, M. He, X. Zhang, and Y. Song, "Facile fabrication of a superhydrophilic–superhydrophobic patterned surface by inkjet printing a sacrificial layer on a

superhydrophilic surface," *RSC Advances*, vol. 6, no. 37, pp. 31470–31475, 2016, doi: 10.1039/C6RA02170K.

[16] W. Feng, L. Li, C. Yang, A. Welle, O. Trapp, and P. A. Levkin, "UV-Induced Tetrazole-Thiol Reaction for Polymer Conjugation and Surface Functionalization," *Angewandte Chemie*, vol. 127, no. 30, pp. 8856–8859, 2015, doi: 10.1002/ange.201502954.

[17] M. Kuang, L. Wang, and Y. Song, "Controllable Printing Droplets for High-Resolution Patterns," *Advanced Materials*, vol. 26, no. 40, pp. 6950–6958, 2014, doi: 10.1002/adma.201305416.

[18] R. Jafari, C. Cloutier, A. Allahdini, and G. Momen, "Recent progress and challenges with 3D printing of patterned hydrophobic and superhydrophobic surfaces," *Int J Adv Manuf Technol*, vol. 103, no. 1, pp. 1225–1238, Jul. 2019, doi: 10.1007/s00170-019-03630-4.

[19] X. Liu *et al.*, "3D Printing of Bioinspired Liquid Superrepellent Structures," *Advanced Materials*, vol. 30, no. 22, p. 1800103, 2018, doi: 10.1002/adma.201800103.

[20] B. S. Kim, S. Shin, S. J. Shin, K. M. Kim, and H. H. Cho, "Micro-nano hybrid structures with manipulated wettability using a two-step silicon etching on a large area," *Nanoscale Res Lett*, vol. 6, no. 1, p. 333, Apr. 2011, doi: 10.1186/1556-276X-6-333.

[21] P. Zhang, B. Peng, J. Wang, and L. Jiang, "Bioinspired Self-Propulsion of Water Droplets at the Convergence of Janus-Textured Heated Substrates," *Advanced Functional Materials*, vol. 29, no. 39, p. 1904535, 2019, doi: 10.1002/adfm.201904535.

[22] J. Yong, F. Chen, Q. Yang, and X. Hou, "Femtosecond laser controlled wettability of solid surfaces," *Soft Matter*, vol. 11, no. 46, pp. 8897–8906, 2015, doi: 10.1039/C5SM02153G.

[23] C. Florian *et al.*, "Controlling the Wettability of Steel Surfaces Processed with Femtosecond Laser Pulses," *ACS Appl. Mater. Interfaces*, vol. 10, no. 42, pp. 36564–36571, Oct. 2018, doi: 10.1021/acsami.8b13908.

[24] R. G. Larson, "Transport and deposition patterns in drying sessile droplets," *AIChE J.*, vol. 60, no. 5, pp. 1538–1571, May 2014, doi: 10.1002/aic.14338.

[25] N. S. Satpathi, K. N. Nampoothiri, and A. K. Sen, "Effects of surface acoustic waves on droplet impact dynamics," *Journal of Colloid and Interface Science*, vol. 641, pp. 499–509, Jul. 2023, doi: 10.1016/j.jcis.2023.03.058.

[26] D. Orejon, K. Sefiane, and M. E. R. Shanahan, "Evaporation of nanofluid droplets with applied DC potential," *Journal of Colloid and Interface Science*, vol. 407, pp. 29–38, Oct. 2013, doi: 10.1016/j.jcis.2013.05.079.

[27] "Droplet Microarrays: From Surface Patterning to High-Throughput Applications - Feng - 2018 - Advanced Materials - Wiley Online Library." Accessed: Mar. 22, 2023. [Online]. Available: https://onlinelibrary-wiley-com.ezproxy.rit.edu/doi/full/10.1002/adma.201706111?casa_token=6Lwh8K6ugKwAAAAA%3A7s0EKwNfQ-NMug-uGYakXutoKX2YIxCDpgYkNNrZT7PvhybDiFECHD9H50nobTF5GW9oid2CAw6YeA

[28] T. Xu *et al.*, "Superwettable Microchips as a Platform toward Microgravity Biosensing," *ACS Nano*, vol. 11, no. 1, pp. 621–626, Jan. 2017, doi: 10.1021/acsnano.6b06896.

[29] L. Zhong, R. Zhang, J. Li, Z. Guo, and H. Zeng, "Efficient Fog Harvesting Based on 1D Copper Wire Inspired by the Plant Pitaya," *Langmuir*, vol. 34, no. 50, pp. 15259–15267, Dec. 2018, doi: 10.1021/acs.langmuir.8b03418.

[30] Y. Hou, M. Yu, X. Chen, Z. Wang, and S. Yao, "Recurrent Filmwise and Dropwise Condensation on a Beetle Mimetic Surface," *ACS Nano*, vol. 9, no. 1, pp. 71–81, Jan. 2015, doi: 10.1021/nn505716b.

[31] A. Mohammad Karim, J. P. Rothstein, and H. P. Kavehpour, “Experimental study of dynamic contact angles on rough hydrophobic surfaces,” *Journal of Colloid and Interface Science*, vol. 513, pp. 658–665, Mar. 2018, doi: 10.1016/j.jcis.2017.11.075.

[32] H. Ko *et al.*, “Active Digital Microfluidic Paper Chips with Inkjet-Printed Patterned Electrodes,” *Advanced Materials*, vol. 26, no. 15, pp. 2335–2340, 2014, doi: 10.1002/adma.201305014.

[33] C. Dixon, A. H. C. Ng, R. Fobel, M. B. Miltenburg, and A. R. Wheeler, “An inkjet printed, roll-coated digital microfluidic device for inexpensive, miniaturized diagnostic assays,” *Lab on a Chip*, vol. 16, no. 23, pp. 4560–4568, 2016, doi: 10.1039/C6LC01064D.

[34] K. A. Bernetski, C. T. Burkhart, K. L. Maki, and M. J. Schertzer, “Characterization of electrowetting, contact angle hysteresis, and adhesion on digital microfluidic devices with inkjet-printed electrodes,” *Microfluid Nanofluid*, vol. 22, no. 9, p. 96, Aug. 2018, doi: 10.1007/s10404-018-2119-4.

[35] Y. Wang, I. Fedin, H. Zhang, and D. V. Talapin, “Direct optical lithography of functional inorganic nanomaterials,” *Science*, vol. 357, no. 6349, pp. 385–388, Jul. 2017, doi: 10.1126/science.aan2958.

[36] M. K. Choi *et al.*, “Wearable red–green–blue quantum dot light-emitting diode array using high-resolution intaglio transfer printing,” *Nat Commun*, vol. 6, no. 1, Art. no. 1, May 2015, doi: 10.1038/ncomms8149.

[37] J. Zhao *et al.*, “Full-color laser displays based on organic printed microlaser arrays,” *Nat Commun*, vol. 10, no. 1, Art. no. 1, Feb. 2019, doi: 10.1038/s41467-019-08834-6.

[38] “Functional surfaces and materials - Fraunhofer IGB,” Fraunhofer Institute for Interfacial Engineering and Biotechnology IGB. Accessed: Nov. 22, 2023. [Online]. Available: https://www.igb.fraunhofer.de/en/research/functional-surfaces-and-materials.html

[39] C. Dorrer and J. Rühe, “Some thoughts on superhydrophobic wetting,” *Soft Matter*, vol. 5, no. 1, pp. 51–61, 2009, doi: 10.1039/B811945G.

[40] S.-Y. Teh, R. Lin, L.-H. Hung, and A. P. Lee, “Droplet microfluidics.,” *Lab on a chip*, vol. 8, no. 2, pp. 198–220, 2008, doi: 10.1039/b715524g.

[41] J. Berthier and K. A. Brakke, *The Physics of Microdroplets*. John Wiley & Sons, 2012.

[42] T. S. Hwa, “Droplet-Based Microfluidics,” 2010.

[43] A. Manz *et al.*, “Planar chips technology for miniaturization and integration of separation techniques into monitoring systems,” *Journal of Chromatography A*, vol. 593, no. 1, pp. 253–258, Feb. 1992, doi: 10.1016/0021-9673(92)80293-4.

[44] C. Yi, C. W. Li, S. Ji, and M. Yang, “Microfluidics technology for manipulation and analysis of biological cells,” *Analytica Chimica Acta*, vol. 560, no. 1–2, pp. 1–23, 2006, doi: 10.1016/j.aca.2005.12.037.

[45] H. A. Stone and S. Kim, “Microfluidics : Basic Issues , Applications , and Challenges,” vol. 47, no. 6, pp. 1250–1254.

[46] H. A. Stone and S. Kim, “Microfluidics: Basic issues, applications, and challenges,” *AIChE Journal*, vol. 47, no. 6, pp. 1250–1254, Jun. 2001, doi: 10.1002/aic.690470602.

[47] P. Gravesen, J. Branebjerg, and O. S. Jensen, “Microfluidics-a review,” *Journal of Micromechanics and Microengineering*, vol. 3, no. 4, pp. 168–182, 1993, doi: 10.1088/0960-1317/3/4/002.

[48] C. Hansen and S. R. Quake, “Microfluidics in structural biology: Smaller, faster... better,” *Current Opinion in Structural Biology*, vol. 13, no. 5, pp. 538–544, 2003, doi: 10.1016/j.sbi.2003.09.010.

[49] D. B. Weibel and G. M. Whitesides, “Applications of microfluidics in chemical biology,” *Current Opinion in Chemical Biology*, vol. 10, no. 6, pp. 584–591, 2006, doi: 10.1016/j.cbpa.2006.10.016.

[50] R. D. Deegan, O. Bakajin, T. F. Dupont, G. Huber, S. R. Nagel, and T. A. Witten, “Contact line deposits in an evaporating drop,” *Phys. Rev. E*, vol. 62, no. 1, pp. 756–765, Jul. 2000, doi: 10.1103/PhysRevE.62.756.

[51] “The separation of two different sized particles in an evaporating droplet - Devlin - 2015 - AIChE Journal - Wiley Online Library.” Accessed: Jun. 28, 2023. [Online]. Available: https://aiche-onlinelibrary-wiley-com.ezproxy.rit.edu/doi/full/10.1002/aic.14977?casa_token=Xlykl-0KVEQAAAAA%3AX4tgbcBKaasdFH1pgHOq16qI0h_NztBiEFP-2WVevoiEd3rv0ILHVQZEGd09GB9qImd7bUn_ZKWmzw

[52] A. B. D. Brown, C. G. Smith, and A. R. Rennie, “Fabricating colloidal particles with photolithography and their interactions at an air-water interface,” *Phys. Rev. E*, vol. 62, no. 1, pp. 951–960, Jul. 2000, doi: 10.1103/PhysRevE.62.951.

[53] T. Kajiya, E. Nishitani, T. Yamaue, and M. Doi, “Piling-to-buckling transition in the drying process of polymer solution drop on substrate having a large contact angle,” *Phys. Rev. E*, vol. 73, no. 1, p. 011601, Jan. 2006, doi: 10.1103/PhysRevE.73.011601.

[54] D. BRUTIN, B. SOBAC, B. LOQUET, and J. SAMPOL, “Pattern formation in drying drops of blood,” *Journal of Fluid Mechanics; Cambridge*, vol. 667, pp. 85–95, Jan. 2011, doi: http://dx.doi.org.ezproxy.rit.edu/10.1017/S0022112010005070.

[55] “High-resolution inkjet printing of electrically conducting lines of silver nanoparticles by edge-enhanced twin-line deposition,” *Appl. Phys. Lett.*, vol. 102, no. 21, p. 214101, May 2013, doi: 10.1063/1.4807782.

[56] J.-H. Kim, S. I. Ahn, J. H. Kim, and W.-C. Zin, “Evaporation of Water Droplets on Polymer Surfaces,” *Langmuir*, vol. 23, no. 11, pp. 6163–6169, May 2007, doi: 10.1021/la0636309.

[57] V. Ragoonanan and A. Aksan, “Heterogeneity in Desiccated Solutions: Implications for Biostabilization,” *Biophysical Journal*, vol. 94, no. 6, pp. 2212–2227, Mar. 2008, doi: 10.1529/biophysj.107.110684.

[58] D. R. Adams, M. Toner, and R. Langer, “Microflow and Crack Formation Patterns in Drying Sessile Droplets of Liposomes Suspended in Trehalose Solutions,” *Langmuir*, vol. 24, no. 15, pp. 7688–7697, Aug. 2008, doi: 10.1021/la703835w.

[59] K. L. Maki and S. Kumar, “Fast Evaporation of Spreading Droplets of Colloidal Suspensions,” *Langmuir*, vol. 27, no. 18, pp. 11347–11363, Sep. 2011, doi: 10.1021/la202088s.

[60] H. Hu and R. G. Larson, “Analysis of the Microfluid Flow in an Evaporating Sessile Droplet,” *Langmuir*, vol. 21, no. 9, pp. 3963–3971, Apr. 2005, doi: 10.1021/la047528s.

[61] N. Denkov, O. Velev, P. Kralchevski, I. Ivanov, H. Yoshimura, and K. Nagayama, “Mechanism of formation of two-dimensional crystals from latex particles on substrates,” *Langmuir*, vol. 8, no. 12, pp. 3183–3190, Dec. 1992, doi: 10.1021/la00048a054.

[62] C. T. Burkhart, K. L. Maki, and M. J. Schertzer, “Effects of Interface Velocity, Diffusion Rate, and Radial Velocity on Colloidal Deposition Patterns Left by Evaporating Droplets,” *J. Heat Transfer*, vol. 139, no. 11, Nov. 2017, doi: 10.1115/1.4036681.

[63] D. Mampallil and H. B. Eral, “A review on suppression and utilization of the coffee-ring effect,” *Advances in Colloid and Interface Science*, vol. 252, pp. 38–54, Feb. 2018, doi: 10.1016/j.cis.2017.12.008.

[64] D. Orejon, K. Sefiane, and M. E. R. Shanahan, “Evaporation of nanofluid droplets with applied DC potential,” *Journal of Colloid and Interface Science*, vol. 407, pp. 29–38, Oct. 2013, doi: 10.1016/j.jcis.2013.05.079.

[65] H. B. Eral, D. M. Augustine, M. H. G. Duits, and F. Mugele, “Suppressing the coffee stain effect: how to control colloidal self-assembly in evaporating drops using electrowetting,” *Soft Matter*, vol. 7, no. 10, pp. 4954–4958, May 2011, doi: 10.1039/C1SM05183K.

[66] D. J. C. M. ’t Mannetje, F. Mugele, and D. van den Ende, “Stick–Slip to Sliding Transition of Dynamic Contact Lines under AC Electrowetting,” *Langmuir*, vol. 29, no. 48, pp. 15116–15121, Dec. 2013, doi: 10.1021/la402761m.
[67] S.-K. Fan, P.-W. Huang, T.-T. Wang, and Y.-H. Peng, “Cross-scale electric manipulations of cells and droplets by frequency-modulated dielectrophoresis and electrowetting,” *Lab Chip*, vol. 8, no. 8, pp. 1325–1331, Jul. 2008, doi: 10.1039/B803204A.
[68] S. K. Wilson and H.-M. D’Ambrosio, “Evaporation of Sessile Droplets,” *Annual Review of Fluid Mechanics*, vol. 55, no. 1, pp. 481–509, 2023, doi: 10.1146/annurev-fluid-031822-013213.
[69] K. Sefiane, “Patterns from drying drops,” *Advances in Colloid and Interface Science*, vol. 206, pp. 372–381, Apr. 2014, doi: 10.1016/j.cis.2013.05.002.
[70] N. D. Patil and R. Bhardwaj, “Recent Developments on Colloidal Deposits Obtained by Evaporation of Sessile Droplets on a Solid Surface,” *J Indian Inst Sci*, vol. 99, no. 1, pp. 143–156, Mar. 2019, doi: 10.1007/s41745-019-0105-9.
[71] Z. Jiang, X. Yang, M. Wu, and X. Man, “The drying of liquid droplets*,” *Chinese Phys. B*, vol. 29, no. 9, p. 096803, Sep. 2020, doi: 10.1088/1674-1056/ab8ac7.
[72] T.-S. Wang and W.-Y. Shi, “Transition of Marangoni convection instability patterns during evaporation of sessile droplet at constant contact line mode,” *International Journal of Heat and Mass Transfer*, vol. 148, p. 119138, Feb. 2020, doi: 10.1016/j.ijheatmasstransfer.2019.119138.
[73] C. T. Burkhart, K. L. Maki, and M. J. Schertzer, “Observation of Contact Line Dynamics in Evaporating Droplets Under the Influence of Electric Fields,” presented at the ASME 2016 14th International Conference on Nanochannels, Microchannels, and Minichannels collocated with the ASME 2016 Heat Transfer Summer Conference and the ASME 2016 Fluids Engineering Division Summer Meeting, American Society of Mechanical Engineers, Jul. 2016, p. V001T04A004-V001T04A004. doi: 10.1115/ICNMM2016-7988.
[74] H. Li, A. Li, Z. Zhao, M. Li, and Y. Song, “Heterogeneous Wettability Surfaces: Principle, Construction, and Applications,” *Small Structures*, vol. 1, no. 2, p. 2000028, 2020, doi: 10.1002/sstr.202000028.
[75] A. G. Hollister, P. Gorai, and E. G. Seebauer, “Surface-based manipulation of point defects in rutile TiO2,” *Applied Physics Letters*, vol. 102, no. 23, p. 231601, Jun. 2013, doi: 10.1063/1.4810073.
[76] S. Semenov, V. M. Starov, R. G. Rubio, H. Agogo, and M. G. Velarde, “Evaporation of sessile water droplets: Universal behaviour in presence of contact angle hysteresis,” *Colloids and Surfaces A: Physicochemical and Engineering Aspects*, vol. 391, no. 1–3, pp. 135–144, Nov. 2011, doi: 10.1016/j.colsurfa.2011.07.013.
[77] D. Orejon, K. Sefiane, and M. E. R. Shanahan, “Stick–Slip of Evaporating Droplets: Substrate Hydrophobicity and Nanoparticle Concentration,” *Langmuir*, vol. 27, no. 21, pp. 12834–12843, Nov. 2011, doi: 10.1021/la2026736.
[78] A. Askounis, D. Orejon, V. Koutsos, K. Sefiane, and M. E. R. Shanahan, “Nanoparticle deposits near the contact line of pinned volatile droplets: size and shape revealed by atomic force microscopy,” *Soft Matter*, vol. 7, no. 9, pp. 4152–4155, 2011, doi: 10.1039/C1SM05241A.
[79] W. D. Ristenpart, P. G. Kim, C. Domingues, J. Wan, and H. A. Stone, “Influence of Substrate Conductivity on Circulation Reversal in Evaporating Drops,” *Phys. Rev. Lett.*, vol. 99, no. 23, p. 234502, Dec. 2007, doi: 10.1103/PhysRevLett.99.234502.
[80] “Analysis of the Effects of Marangoni Stresses on the Microflow in an Evaporating Sessile Droplet | Langmuir.” Accessed: Jun. 28, 2023. [Online]. Available: https://pubs-acs-org.ezproxy.rit.edu/doi/full/10.1021/la0475270?casa_token=JAgQchr7DnoAAAAA%3APBh

bpqDwGoFHiNrOOei93FrgAfBqkCHLFOB7XVxDIJXZpds11UDOVDWLghb5SNafj-zcD3EowTKYrw

[81] G. Corkidi, F. Montoya, G. Hernández-Cruz, M. Vargas, J. L. Luviano-Ortíz, and E. Ramos, "Evaporation dynamics and sedimentation pattern of a sessile particle laden water droplet," *Exp Fluids*, vol. 57, no. 6, p. 99, May 2016, doi: 10.1007/s00348-016-2182-0.

[82] K. A. Raman, R. K. Jaiman, T.-S. Lee, and H.-T. Low, "Lattice Boltzmann simulations of droplet impact onto surfaces with varying wettabilities," *International Journal of Heat and Mass Transfer*, vol. 95, pp. 336–354, Apr. 2016, doi: 10.1016/j.ijheatmasstransfer.2015.11.088.

[83] U. Thiele, "Patterned deposition at moving contact lines," *Advances in Colloid and Interface Science*, vol. 206, pp. 399–413, Apr. 2014, doi: 10.1016/j.cis.2013.11.002.

[84] P. J. Yunker, T. Still, M. A. Lohr, and A. G. Yodh, "Suppression of the coffee-ring effect by shape-dependent capillary interactions," *Nature*, vol. 476, no. 7360, pp. 308–311, Aug. 2011, doi: 10.1038/nature10344.

[85] V. R. Dugyala and M. G. Basavaraj, "Control over Coffee-Ring Formation in Evaporating Liquid Drops Containing Ellipsoids," *Langmuir*, vol. 30, no. 29, pp. 8680–8686, Jul. 2014, doi: 10.1021/la500803h.

[86] S. P. Molchanov, V. I. Roldughin, and I. A. Chernova-Kharaeva, "Three scenarios of evaporation of microliter droplets of dispersions and structure of formed ring-shaped deposits," *Colloid J*, vol. 77, no. 6, pp. 770–779, Nov. 2015, doi: 10.1134/S1061933X15060162.

[87] S. P. Molchanov, V. I. Roldughin, I. A. Chernova-Kharaeva, and I. N. Senchikhin, "The Effect of Electrokinetic Potential on Evaporation of Colloidal Dispersion Droplets," *Colloid J*, vol. 81, no. 2, pp. 136–145, Mar. 2019, doi: 10.1134/S1061933X19020091.

[88] R. Bhardwaj, X. Fang, and D. Attinger, "Pattern formation during the evaporation of a colloidal nanoliter drop: a numerical and experimental study," *New J. Phys.*, vol. 11, no. 7, p. 075020, 2009, doi: 10.1088/1367-2630/11/7/075020.

[89] P. J. Yunker, M. A. Lohr, T. Still, A. Borodin, D. J. Durian, and A. G. Yodh, "Effects of Particle Shape on Growth Dynamics at Edges of Evaporating Drops of Colloidal Suspensions," *Phys. Rev. Lett.*, vol. 110, no. 3, p. 035501, Jan. 2013, doi: 10.1103/PhysRevLett.110.035501.

[90] J. C. Loudet, A. G. Yodh, and B. Pouligny, "Wetting and Contact Lines of Micrometer-Sized Ellipsoids," *Phys. Rev. Lett.*, vol. 97, no. 1, p. 018304, Jul. 2006, doi: 10.1103/PhysRevLett.97.018304.

[91] R. Bhardwaj, X. Fang, P. Somasundaran, and D. Attinger, "Self-Assembly of Colloidal Particles from Evaporating Droplets: Role of DLVO Interactions and Proposition of a Phase Diagram," *Langmuir*, vol. 26, no. 11, pp. 7833–7842, Jun. 2010, doi: 10.1021/la9047227.

[92] J. R. Moffat, K. Sefiane, and M. E. R. Shanahan, "Effect of TiO2 Nanoparticles on Contact Line Stick−Slip Behavior of Volatile Drops," *J. Phys. Chem. B*, vol. 113, no. 26, pp. 8860–8866, Jul. 2009, doi: 10.1021/jp902062z.

[93] Q. Li, P. Zhou, and H. J. Yan, "Pinning–Depinning Mechanism of the Contact Line during Evaporation on Chemically Patterned Surfaces: A Lattice Boltzmann Study," *Langmuir*, vol. 32, no. 37, pp. 9389–9396, Sep. 2016, doi: 10.1021/acs.langmuir.6b01490.

[94] Y. Li, Q. Yang, M. Li, and Y. Song, "Rate-dependent interface capture beyond the coffee-ring effect," *Scientific Reports*, vol. 6, no. April, p. 24628, 2016, doi: 10.1038/srep24628.

[95] H. Kim, N. Belmiloud, and P. W. Mertens, "Non-uniformly receding contact line breaks axisymmetric flow patterns," *Eur. Phys. J. Spec. Top.*, vol. 229, no. 10, pp. 1771–1784, Sep. 2020, doi: 10.1140/epjst/e2020-900281-3.

[96] H. P. Jansen, H. J. W. Zandvliet, and E. S. Kooij, “Evaporation of elongated droplets on chemically stripe-patterned surfaces,” *International Journal of Heat and Mass Transfer*, vol. 82, pp. 537–544, Mar. 2015, doi: 10.1016/j.ijheatmasstransfer.2014.11.028.
[97] M. Taniguchi and G. Belfort, “Correcting for Surface Roughness: Advancing and Receding Contact Angles,” *Langmuir*, vol. 18, no. 16, pp. 6465–6467, Aug. 2002, doi: 10.1021/la020145e.
[98] “Characterization of Particle Transport and Deposition Due to Heterogeneous Dewetting on Low-Cost Inkjet-Printed Devices | Langmuir.” Accessed: Nov. 24, 2023. [Online]. Available: https://pubs-acs-org.ezproxy.rit.edu/doi/full/10.1021/acs.langmuir.3c02224?casa_token=2H6hN__MW-QAAAAA%3AjTL8dr3LA-JeRDePvfeXZoaazKDs2wVcCc0gHkHNb8bitslMOGfHkL_dUauvW-yARCvt_CkMsDMzlw
[99] D. Kim, S. Jeong, B. K. Park, and J. Moon, “Direct writing of silver conductive patterns: Improvement of film morphology and conductance by controlling solvent compositions,” *Applied Physics Letters*, vol. 89, no. 26, p. 264101, Dec. 2006, doi: 10.1063/1.2424671.
[100] R. D. Deegan, O. Bakajin, T. F. Dupont, G. Huber, S. R. Nagel, and T. A. Witten, “Capillary flow as the cause of ring stains from dried liquid drops,” *Nature*, vol. 389, no. 6653, pp. 827–829, Oct. 1997, doi: 10.1038/39827.
[101] F. Mugele and J.-C. Baret, “Electrowetting: from basics to applications,” *J. Phys.: Condens. Matter*, vol. 17, no. 28, p. R705, 2005, doi: 10.1088/0953-8984/17/28/R01.
[102] F. Mugele, “Fundamental challenges in electrowetting: from equilibrium shapes to contact angle saturation and drop dynamics,” *Soft Matter*, vol. 5, no. 18, pp. 3377–3384, Sep. 2009, doi: 10.1039/B904493K.
[103] J. G. Lee and H. J. Eom, “Magnetostatic potential distribution through a circular aperture in a thick conducting plane,” *IEEE Transactions on Electromagnetic Compatibility*, vol. 40, no. 2, pp. 97–99, May 1998, doi: 10.1109/15.673613.
[104] P.-M. Lee *et al.*, “An In-situ Correction Method of Position Error for an Autonomous Underwater Vehicle Surveying the Sea Floor,” *International Journal of Ocean System Engineering*, vol. 1, no. 2, pp. 60–67, 2011, doi: 10.5574/IJOSE.2011.1.2.060.
[105] J. Bandy, Q. Zhang, and G. Cao, “Electrophoretic Deposition of Titanium Oxide Nanoparticle Films for Dye-Sensitized Solar Cell Applications,” *Materials Sciences and Applications*, vol. 2, no. 10, Art. no. 10, Oct. 2011, doi: 10.4236/msa.2011.210193.
[106] A. H. Jayatissa, “Electrophoresis coating of titanium dioxide nanoparticles in anodic nanotemplate,” in *Nanofabrication: Technologies, Devices, and Applications*, International Society for Optics and Photonics, Jan. 2005, pp. 400–405. doi: 10.1117/12.571944.
[107] S. K. Cho, Y. Zhao, and C.-J. “CJ” Kim, “Concentration and binary separation of micro particles for droplet-based digital microfluidics,” *Lab Chip*, vol. 7, no. 4, pp. 490–498, Mar. 2007, doi: 10.1039/B615665G.
[108] B. H. W. Hendriks, S. Kuiper, M. A. J. VAN As, C. A. Renders, and T. W. Tukker, “Electrowetting-Based Variable-Focus Lens for Miniature Systems,” *OPT REV*, vol. 12, no. 3, pp. 255–259, May 2005, doi: 10.1007/s10043-005-0255-z.
[109] S. Kuiper and B. H. W. Hendriks, “Variable-focus liquid lens for miniature cameras,” *Appl. Phys. Lett.*, vol. 85, no. 7, pp. 1128–1130, Aug. 2004, doi: 10.1063/1.1779954.
[110] R. B. Fair, “Digital microfluidics: is a true lab-on-a-chip possible?,” *Microfluid Nanofluid*, vol. 3, no. 3, pp. 245–281, Jun. 2007, doi: 10.1007/s10404-007-0161-8.
[111] E. M. Miller and A. R. Wheeler, “Digital bioanalysis,” *Anal Bioanal Chem*, vol. 393, no. 2, pp. 419–426, Jan. 2009, doi: 10.1007/s00216-008-2397-x.

[112] H. Lee, S. Yun, S. H. Ko, and K. H. Kang, “An electrohydrodynamic flow in ac electrowetting,” *Biomicrofluidics*, vol. 3, no. 4, p. 044113, Dec. 2009, doi: 10.1063/1.3274511.

[113] J. S. Hong, S. H. Ko, K. H. Kang, and I. S. Kang, “A numerical investigation on AC electrowetting of a droplet,” *Microfluid Nanofluid*, vol. 5, no. 2, pp. 263–271, Aug. 2008, doi: 10.1007/s10404-007-0246-4.